

RECEIVED: March 15, 2022

REVISED: June 2, 2022

ACCEPTED: June 8, 2022

PUBLISHED: July 8, 2022

Amplitude analysis and branching fraction measurement of $D_s^+ \rightarrow K^- K^+ \pi^+ \pi^+ \pi^-$



The BESIII collaboration

E-mail: besiii-publications@ihep.ac.cn

ABSTRACT: Using e^+e^- annihilation data corresponding to a total integrated luminosity of 6.32 fb^{-1} collected at the center-of-mass energies between 4.178 and 4.226 GeV with the BESIII detector, we perform an amplitude analysis of the decay $D_s^+ \rightarrow K^- K^+ \pi^+ \pi^+ \pi^-$ and determine the relative fractions and phases of different intermediate processes. Absolute branching fraction of $D_s^+ \rightarrow K^- K^+ \pi^+ \pi^+ \pi^-$ decay is measured to be $(6.60 \pm 0.47_{\text{stat.}} \pm 0.38_{\text{syst.}}) \times 10^{-3}$. The dominant intermediate process is $D_s^+ \rightarrow a_1(1260)^+ \phi, \phi \rightarrow K^- K^+, a_1(1260)^+ \rightarrow \rho \pi^+, \rho \rightarrow \pi^+ \pi^-$, with a branching fraction of $(5.15 \pm 0.41_{\text{stat.}} \pm 0.32_{\text{syst.}}) \times 10^{-3}$.

KEYWORDS: Branching fraction, Charm Physics, e^+e^- Experiments, Particle and Resonance Production

ARXIV EPRINT: [2203.06688](https://arxiv.org/abs/2203.06688)

Contents

1	Introduction	1
2	Detector and data sets	2
3	Event selection	4
4	Amplitude analysis	5
4.1	Further selection criteria	5
4.2	Fit method	6
4.2.1	Blatt-Weisskopf barriers	8
4.2.2	Propagator	8
4.2.3	Spin factors	9
4.3	Fit results	10
4.4	Systematic uncertainties for amplitude analysis	11
5	Branching fraction measurement	14
6	Summary	18
A	All other tested amplitudes	20
	The BESIII collaboration	23

1 Introduction

The hadronic decays of D_s^+ mesons are dominated by two-body processes [1], such as $D_s^+ \rightarrow PP, VP, VS, VV, AP$ and AV , where P, V, S and A denote pseudo-scalar, vector, scalar and axial-vector mesons, respectively. The branching fractions (BFs) of most of these decays can be calculated theoretically [2], even if the non-perturbative contributions, such as final-state interactions, make some of them hard to predict. Therefore, BFs measurements of the D_s^+ two-body decays are important to test the theoretical calculations and can be helpful to understand the decay mechanisms of D_s^+ mesons. Up to now, there are no references to studies focusing on $D_s^+ \rightarrow AV$ decays. Among them, the process $D_s^+ \rightarrow a_1(1260)^+\phi$, which is mediated via the diagram in figure 1, can be studied in the $D_s^+ \rightarrow K^-K^+\pi^+\pi^+\pi^-$ decay.

Moreover, experimental study of $D_s^+ \rightarrow K^+K^-\pi^+\pi^+\pi^-$ is also helpful to clarify the tension observed in the ratio $R(D^*) \equiv \mathcal{B}(B \rightarrow D^*\tau^+\nu_\tau)/\mathcal{B}(B \rightarrow D^*\ell^+\nu_\ell)$ ($\ell = e, \mu$), with an average of $0.295 \pm 0.011 \pm 0.008$ provided by the Heavy Flavor Averaging Group, which differs from the Standard Model prediction of 0.258 ± 0.005 by 2.6 standard deviations [3].¹ This

¹Updated results available at <https://hflav-eos.web.cern.ch/hflav-eos/semi/spring19/html/RDsDstar/RDRDs.html>.

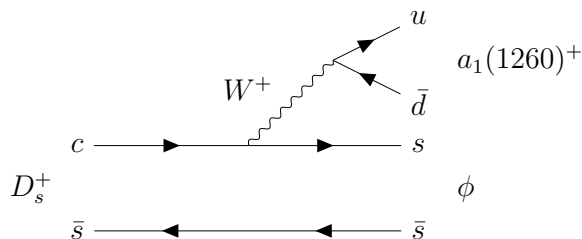


Figure 1. Feynman diagram of $D_s^+ \rightarrow a_1(1260)^+ \phi$.

Decay mode	E687 [6]		FOCUS [7]	
	fitted yield	BF ratio	fitted yield	BF ratio
$\frac{\Gamma(D_s^+ \rightarrow K^- K^+ \pi^+ \pi^+ \pi^-)}{\Gamma(D_s^+ \rightarrow K^- K^+ \pi^+)}$	240 ± 30	$0.188 \pm 0.036 \pm 0.040$	136 ± 14	$0.150 \pm 0.019 \pm 0.025$
$\frac{\Gamma(D_s^+ \rightarrow \phi \pi^+ \pi^+ \pi^-)}{\Gamma(D_s^+ \rightarrow K^- K^+ \pi^+)}$	75 ± 13	$0.280 \pm 0.060 \pm 0.010$	40 ± 8	$0.249 \pm 0.024 \pm 0.021$

Table 1. The fitted yields and BF ratios for the previous measurements by E687 and FOCUS experiments. All BF ratios are inclusive of subresonant modes.

hints a possible violation of the lepton flavor universality. However, the $R(D^*)$ measurement at LHCb experiment suffers from a large systematic uncertainty due to the limited knowledge of the inclusive $D_s^+ \rightarrow \pi^+ \pi^+ \pi^- X$ decay [4, 5], where the decay of $B \rightarrow D^{*-} D_s^+, D_s^+ \rightarrow \pi^+ \pi^+ \pi^- X$ is main background in the decay chain $B^0 \rightarrow D^{*-} \tau^+ \nu_\tau, \tau^+ \rightarrow \pi^+ \pi^+ \pi^- X$. A precise measurement of the branching fraction (BF) of $D_s^+ \rightarrow K^- K^+ \pi^+ \pi^+ \pi^-$, which is one of the dominant processes in $D_s^+ \rightarrow \pi^+ \pi^+ \pi^- X$, can provide a useful input to improve the precision of $R(D^*)$.

The E687 [6] and FOCUS [7] experiments reported the fitted yields and BFs of $D_s^+ \rightarrow K^- K^+ \pi^+ \pi^+ \pi^-$ relative to $D_s^+ \rightarrow K^+ K^- \pi^+$, as shown in table 1. By performing an analysis of the resonant substructure in the decay $D_s^+ \rightarrow K^- K^+ \pi^+ \pi^+ \pi^-$, the FOCUS experiment observed that the decay proceeds primarily through a quasi-two-body decay involving an $a_1(1260)^+$ resonance. In this paper, we perform the first amplitude analysis, as well as measuring the absolute BF of $D_s^+ \rightarrow K^- K^+ \pi^+ \pi^+ \pi^-$, by using the 6.32 fb^{-1} data samples collected by the BESIII detector at the center-of-mass energies (\sqrt{s}) from 4.178 to 4.226 GeV. More precise measurements and a detailed study of the decay structure are expected. Charge conjugate states are always implied throughout this paper.

2 Detector and data sets

The BESIII detector [8] records symmetric e^+e^- collisions provided by the BEPCII storage ring [9], which operates in the center-of-mass energy range from $\sqrt{s} = 2.00$ to $\sqrt{s} = 4.95$ GeV [10]. The cylindrical core of the BESIII detector covers 93% of the full solid angle and consists of a helium-based multilayer drift chamber (MDC), a plastic scintillator time-of-flight system (TOF), and a CsI(Tl) electromagnetic calorimeter (EMC), which are all enclosed in a superconducting solenoidal magnet providing a 1.0 T magnetic field. The

\sqrt{s} (GeV)	\mathcal{L}_{int} (pb ⁻¹) [14]	M_{rec} (GeV/c ²)
4.178	3189.0±0.2±31.9	[2.050, 2.180]
4.189	526.7±0.1±2.2	[2.048, 2.190]
4.199	526.0±0.1±2.1	[2.046, 2.200]
4.209	517.1±0.1±1.8	[2.044, 2.210]
4.219	514.6±0.1±1.8	[2.042, 2.220]
4.226	1056.4±0.1±7.0	[2.040, 2.220]

Table 2. The integrated luminosities (\mathcal{L}_{int}) and the requirements on M_{rec} for various center-of-mass energies. The definition of M_{rec} is given in eq. (3.1). The first and second uncertainties are statistical and systematic, respectively.

solenoid is supported by an octagonal flux-return yoke with resistive plate counter muon identification modules interleaved with steel. The charged-particle momentum resolution at 1 GeV/c is 0.5%, and the dE/dx resolution is 6% for electrons from Bhabha scattering. The EMC measures photon energies with a resolution of 2.5% (5%) at 1 GeV in the barrel (end cap) region. The time resolution in the TOF barrel region is 68 ps, while that in the end cap region is 110 ps. The end cap TOF system was upgraded in 2015 using multi-gap resistive plate chamber technology, providing a time resolution of 60 ps [11–13].

The data samples used in this analysis contain a total integrated luminosity of 6.32 fb⁻¹ collected at the center-of-mass energies between 4.178 and 4.226 GeV. The integrated luminosity of each data sample is shown in table 2 [14]. The data sets are organized into three sample groups, 4.178 GeV, 4.189–4.219 GeV, and 4.226 GeV, which were acquired during the same year under consistent running conditions.

Inclusive Monte Carlo (MC) samples that are 40 times larger than the data sets are produced at the center-of-mass energies between 4.178 and 4.226 GeV with a GEANT4-based [15] MC package, which includes the geometric description of the BESIII detector and the detector response. These samples are used to determine detection efficiencies and to estimate backgrounds. The samples include the production of open charm processes, the initial-state radiation (ISR) production of vector charmonium(-like) states and the continuum processes incorporated in KKMC [16, 17]. The known decay modes are modeled with EVTGEN [18, 19] using the BFs taken from the Particle Data Group (PDG) [1], and the remaining unknown charmonium decays are modeled with LUNDCHARM [20, 21]. Final state radiation (FSR) from charged final state particles is incorporated using PHOTOS [22]. A phase-space (PHSP) MC sample is produced with the $D_s^+ \rightarrow K^- K^+ \pi^+ \pi^+ \pi^-$ generated with a uniform distribution and is used to extract the detection efficiency maps. Initially, the PHSP MC sample is used to calculate the normalization integral used in the determination of the amplitude model parameters in the fit to data. Then, the signal MC sample is re-generated with the D_s^+ meson decaying to $K^- K^+ \pi^+ \pi^+ \pi^-$ using the amplitude model. It is used to evaluate the fit quality and estimate the systematic uncertainty.

Tag mode	Mass window (GeV/ c^2)
$D_s^- \rightarrow K_S^0 K^-$	[1.948, 1.991]
$D_s^- \rightarrow K^+ K^- \pi^-$	[1.950, 1.986]
$D_s^- \rightarrow K_S^0 K^+ \pi^0$	[1.946, 1.987]
$D_s^- \rightarrow K^+ K^- \pi^- \pi^0$	[1.947, 1.982]
$D_s^- \rightarrow K_S^0 K^- \pi^- \pi^+$	[1.958, 1.980]
$D_s^- \rightarrow K_S^0 K^+ \pi^- \pi^-$	[1.953, 1.983]
$D_s^- \rightarrow \pi^- \eta'_{\pi^+\pi^-} \eta_{\gamma\gamma}$	[1.940, 1.996]
$D_s^- \rightarrow \pi^- \eta_{\gamma\gamma}$	[1.930, 2.000]

Table 3. Requirements on M_{tag} for various tag modes, where the η and η' subscripts denote the decay modes used to reconstruct these particles.

3 Event selection

The data samples were collected just above the $D_s^{*\pm} D_s^\mp$ threshold. In this energy region, pairs of $D_s^{*\pm} D_s^\mp$ mesons are produced copiously; subsequently, the $D_s^{*\pm}$ meson predominantly decays to γD_s^\pm with a branching fraction of $(93.5 \pm 0.7)\%$ [1]. The tag method [23] allows to select clean signal samples, providing the opportunity to perform amplitude analyses and to measure the absolute BFs of the hadronic D_s^+ meson decays. In the tag method, a single-tag (ST) candidate requires only one of the D_s^\pm mesons to be reconstructed via a hadronic decay. A double-tag (DT) candidate has both $D_s^+ D_s^-$ mesons reconstructed, requiring the D_s^+ meson decaying to the signal mode $D_s^+ \rightarrow K^- K^+ \pi^+ \pi^+ \pi^-$ and the D_s^- meson decaying to the eight tag modes listed in table 3. The reconstruction of π^\pm , K^\pm , K_S^0 , π^0 , η , and η' particles in the final state is discussed below.

All charged tracks reconstructed in the MDC must satisfy the condition $|\cos\theta| < 0.93$, where θ is the polar angle with respect to the direction of the positron beam. For charged tracks not originating from K_S^0 decays, the distance of closest approach to the interaction point is required to be less than 10 cm along the beam direction and less than 1 cm in the plane perpendicular to the beam. Particle identification (PID) for charged tracks combines the measurements of the dE/dx in the MDC and the time of flight in the TOF to form likelihoods $\mathcal{L}(h)$ ($h = K, \pi$) for each hadron h hypothesis. Charged kaons and pions are identified by comparing the likelihoods for the two hypotheses, $\mathcal{L}(K) > \mathcal{L}(\pi)$ and $\mathcal{L}(\pi) > \mathcal{L}(K)$, respectively.

The K_S^0 candidates are selected by looping over all pairs of tracks with opposite charges, whose distances to the interaction point along the beam direction are within 20 cm. A primary vertex and a secondary vertex are reconstructed and the decay length between the two vertexes is required to be greater than twice its uncertainty. This requirement is not applied for the $D_s^- \rightarrow K_S^0 K^-$ decay since the combinatorial background is low. Candidate K_S^0 particles are required to have the χ^2 of the vertex fit less than 100 and an invariant mass of the $\pi^+ \pi^-$ pair ($M_{\pi^+\pi^-}$) in the range [0.487, 0.511] GeV/ c^2 . To prevent an event being

double counted in the $D_s^- \rightarrow K_s^0 K^-$ and $D_s^- \rightarrow K^- \pi^+ \pi^-$ selections, the value of $M_{\pi^+\pi^-}$ is required to be outside of the mass range $[0.487, 0.511]$ GeV/c^2 for the $D_s^- \rightarrow K^- \pi^+ \pi^-$ decay.

Photon candidates are identified using showers in the EMC. The deposited energy of each shower must be more than 25 MeV in the barrel region ($|\cos\theta| < 0.80$) and more than 50 MeV in the end cap region ($0.86 < |\cos\theta| < 0.92$). The angle between the position of each shower in the EMC and the closest extrapolated charged track must be greater than 10 degrees to exclude showers that originate from charged tracks. The difference between the EMC time and the event start time is required to be within $[0, 700]$ ns to suppress electronic noise and showers unrelated to the event.

The π^0 (η) candidates are reconstructed through $\pi^0 \rightarrow \gamma\gamma$ ($\eta \rightarrow \gamma\gamma$) decays, with at least one photon falling in the barrel region. The invariant mass of the photon pair for π^0 and η candidates must be in the ranges $[0.115, 0.150]$ GeV/c^2 and $[0.500, 0.570]$ GeV/c^2 , respectively, which are about three times the mass resolution around their known masses. A kinematic fit that constrains the $\gamma\gamma$ invariant mass to the π^0 or η known mass [1] is performed to improve the mass resolution and the χ^2 is required to be less than 30. The η' candidates are formed from the $\pi^+\pi^-\eta$ combinations with an invariant mass within a range of $[0.946, 0.970]$ GeV/c^2 .

Eight tag modes are reconstructed and the corresponding mass windows on the tagging D_s^- mass (M_{tag}) are listed in table 3. The signal D_s^+ candidates, whose M_{rec} lies within the mass windows listed in table 2, are retained for further studies, considering the quantity M_{rec} defined as

$$M_{\text{rec}} = \sqrt{\left(E_{\text{cm}} - \sqrt{|\vec{p}_{D_s^-}|^2 + m_{D_s^-}^2}\right)^2 - |\vec{p}_{D_s^-}|^2}, \quad (3.1)$$

where E_{cm} is the energy of the initial state calculated from the beam energy, $\vec{p}_{D_s^-}$ is the three-momentum of the D_s^- candidate in the e^+e^- center-of-mass frame, and $m_{D_s^-}$ is the D_s^- known mass [1].

4 Amplitude analysis

4.1 Further selection criteria

The following selection criteria are further applied in order to obtain signal samples with high purity for the amplitude analysis. The selection criteria discussed in this section are not used in the BF measurements.

A six-constraint (6C) kinematic fit is performed to the process $e^+e^- \rightarrow D_s^{*\pm} D_s^\mp \rightarrow \gamma D_s^+ D_s^-$, assuming D_s^- decaying to one of the tag modes and D_s^+ decaying to the signal mode ($K^- K^+ \pi^+ \pi^+ \pi^-$) with two hypotheses: the signal D_s^+ comes from a D_s^{*+} or the D_s^- comes from a D_s^{*-} . The total four-momentum is constrained to the initial four-momentum of the e^+e^- system, and the invariant masses of tag D_s^- and $D_s^{*\pm}$ candidates are constrained to the corresponding known masses. The best $D_s^{*\pm} D_s^\mp$ combination with the minimum χ_{6C}^2 is selected. Then, a seventh constraint of the signal D_s^+ invariant mass is added to the 6C kinematic fit, in order to ensure that all the events fall into the PHSP boundary. The updated four-momenta obtained from the seven-constraint kinematic fit of the final particles are used to perform the amplitude analysis.

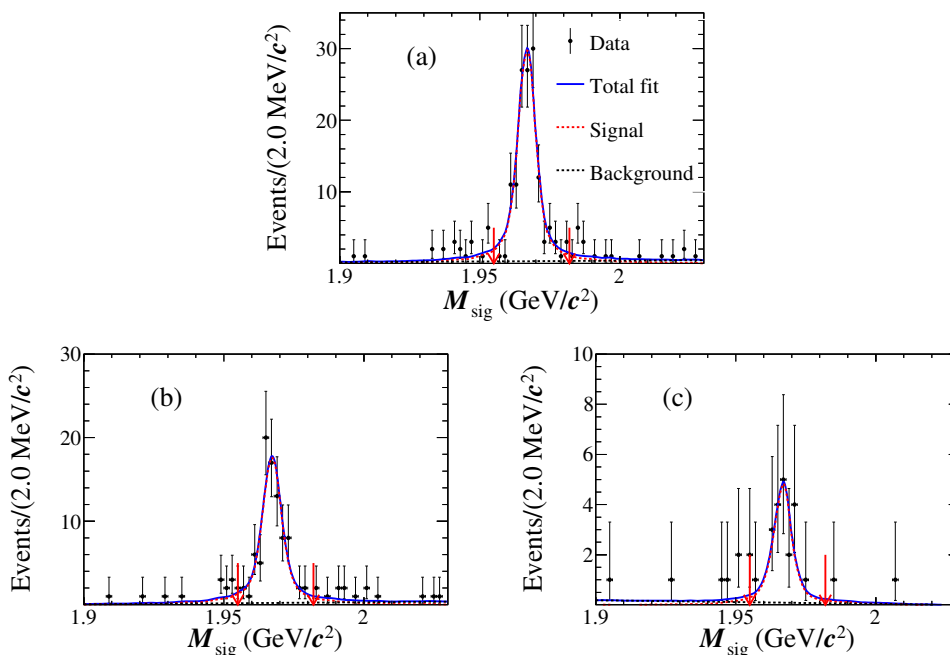


Figure 2. Fits to the M_{sig} distributions of the data samples at $\sqrt{s} =$ (a) 4.178 GeV, (b) 4.189–4.219 GeV and (c) 4.226 GeV. The black points with error bars are data. The blue solid lines are the total fits. The red dotted and the black dashed lines are the fitted signal and background, respectively. The pairs of red arrows indicate the signal regions.

The signal region of the D_s^+ invariant mass for the $D_s^+ \rightarrow K^- K^+ \pi^+ \pi^+ \pi^-$ decay is defined as $[1.955, 1.982] \text{ GeV}/c^2$. The π^+ with lower invariant mass of $\pi^+ \pi^-$ pair is denoted as π_1^+ and the other π^+ as π_2^+ . If the invariant mass of $\pi_1^+ \pi^-$ or $\pi_2^+ \pi^-$ satisfies the selection of K_S^0 mesons, these candidates are vetoed. There are background events from $D_s^+ \rightarrow K^- K^+ \pi^+ \pi^0$, $\pi^0 \rightarrow e^+ e^- \gamma$, in which the $e^+ e^-$ pair is misidentified as a $\pi^+ \pi^-$ pair. We use $\cos\theta(\pi_1^+ \pi^-) > 0.985$ to suppress this kind of background, where θ is the opening angle between the momenta of π^- and π_1^+ .

Figure 2 shows the fits to the invariant-mass distributions of the accepted signal D_s^+ candidates (M_{sig}) for various data samples. The signal is described by a MC-simulated shape convolved with a Gaussian function, and the background is described by a linear function. Finally, a mass window $[1.955, 1.982] \text{ GeV}/c^2$ is applied on the signal D_s^+ candidates. There are 137, 84 and 22 events retained for the amplitude analysis with signal purities $(96.9 \pm 1.5)\%$, $(96.7 \pm 2.0)\%$ and $(94.9 \pm 4.7)\%$ for the data samples at $\sqrt{s} = 4.178, 4.189\text{--}4.219$ and 4.226 GeV, respectively.

4.2 Fit method

The amplitude analysis of $D_s^+ \rightarrow K^- K^+ \pi^+ \pi^+ \pi^-$ decay is performed by using an unbinned maximum likelihood fit. The isobar formalism is used to model the total amplitude. For the decay of $D_s^+ \rightarrow K^- K^+ \pi^+ \pi^+ \pi^-$, there are three intermediate resonances at most. For example, $D_s \rightarrow R_1 R_2$, $R_1 \rightarrow R_3 P_1$, $R_3 \rightarrow P_2 P_3$, $R_2 \rightarrow P_4 P_5$, where R_1, R_2 , and R_3 are

intermediate resonances. The amplitude of the n^{th} intermediate process (\mathcal{A}_n) is given by:

$$\mathcal{A}_n(p_j) = P_n^1(m_1)P_n^2(m_2)P_n^3(m_3)S_n(p_j)F_n^1(p_j)F_n^2(p_j)F_n^3(p_j)F_n^{D_s}(p_j), \quad (4.1)$$

where p_j is the set of the final state particles' four momenta, the index j refers to the different particles in the final states, the indices 1, 2 and 3 correspond to the three intermediate resonances. In the amplitude, $S_n(p_j)$ is the spin factor, $F_n^{1,2,3}(p_j)$ and $F_n^{D_s}(p_j)$ are the Blatt-Weisskopf barrier factors for the intermediate resonances and D_s^+ , and $P^{1,2,3}$ are the propagators for the intermediate resonances. For the non-resonance (NR) amplitude $D_s^+ \rightarrow (K^-K^+\pi^+\pi^+\pi^-)_{\text{NR}}$, we use $\mathcal{A}_n(p_j) = 1$. The total amplitude \mathcal{M} is the coherent sum of the amplitudes of the intermediate processes, $\mathcal{M}(p_j) = \sum c_n \mathcal{A}_n(p_j)$, where $c_n = \rho_n e^{i\phi_n}$ is the corresponding complex coefficient. The magnitude ρ_n and phase ϕ_n will be determined in the likelihood fit. The two identical final state π^+ 's are symmetrised in the model. The signal probability density function (PDF) $f_S(p_j)$ is given by:

$$f_S(p_j) = \frac{\epsilon(p_j)|\mathcal{M}(p_j)|^2 R_5(p_j)}{\int \epsilon(p_j)|\mathcal{M}(p_j)|^2 R_5(p_j) dp_j}, \quad (4.2)$$

where $\epsilon(p_j)$ is the detection efficiency parameterised in terms of the final four-momenta p_j and $R_5(p_j)$ is the PHSP element of five-body decays. In the numerator of eq. (4.2), $\epsilon(p_j)$ and $R_5(p_j)$ terms are independent of the fitted variables, so they are regarded as constant terms in the fit. The normalization integrals are determined by a MC integration:

$$\int \epsilon(p_j)|\mathcal{M}(p_j)|^2 R_5(p_j) dp_j \approx \frac{1}{N_{\text{gen}}} \sum_{k_{\text{MC}}}^{N_{\text{MC}}} \frac{|\mathcal{M}(p_j^{k_{\text{MC}}})|^2}{|\mathcal{M}^{\text{gen}}(p_j^{k_{\text{MC}}})|^2}, \quad (4.3)$$

where k_{MC} is the index of the $k_{\text{MC}}^{\text{th}}$ event of the MC sample, N_{gen} is the number of the generated MC events and N_{MC} is the number of the selected MC events. The $\mathcal{M}^{\text{gen}}(p_j)$ is the PDF used to generate the MC samples in the MC integration. The computational efficiency of the MC integration is significantly improved by evaluating the normalization integral with signal MC samples, which intrinsically take into account the event selection acceptance and the detection resolution.

The PID and tracking efficiencies are studied using control samples of $e^+e^- \rightarrow K^+K^-K^+K^-$, $e^+e^- \rightarrow K^+K^-\pi^+\pi^-$, $e^+e^- \rightarrow K^+K^-\pi^+\pi^-\pi^0$, $e^+e^- \rightarrow \pi^+\pi^-\pi^+\pi^-$, and $e^+e^- \rightarrow \pi^+\pi^-\pi^+\pi^-\pi^0$ decays. The effect from the tracking and PID differences between data and simulation is considered by multiplying the weight of the MC event by a factor γ_ϵ , which is calculated as:

$$\gamma_\epsilon(p_j) = \prod_i \frac{\epsilon_{i,\text{data}}(p_j)}{\epsilon_{i,\text{MC}}(p_j)}, \quad (4.4)$$

where i refers to tracking or PID, $\epsilon_{i,\text{data}}(p_j)$ and $\epsilon_{i,\text{MC}}(p_j)$ is the tracking or PID efficiency as a function of the momenta of the daughter particles for data and MC, respectively. By weighting each signal MC event with γ_ϵ , the MC integration is given by:

$$\int \epsilon(p_j)|\mathcal{M}(p_j)|^2 R_5(p_j) dp_j \approx \frac{1}{N_{\text{MC}}} \sum_{k_{\text{MC}}}^{N_{\text{MC}}} \frac{\gamma_\epsilon(p_j^{k_{\text{MC}}})|\mathcal{M}(p_j^{k_{\text{MC}}})|^2}{|\mathcal{M}^{\text{gen}}(p_j^{k_{\text{MC}}})|^2}. \quad (4.5)$$

The contribution from the background is subtracted in the likelihood calculation by assigning a negative weight to the background events. The log-likelihood function is written as:

$$\ln \mathcal{L} = \sum_k^{N_{\text{data}}} \ln f_S(p_j^k) - \sum_{k'}^{N_{\text{bkg}}} w_{k'}^{\text{bkg}} \ln f_S(p_j^{k'}), \quad (4.6)$$

where N_{data} is the number of candidate events in data, $w_{k'}^{\text{bkg}}$ and N_{bkg} are the background weight and the number of simulated background events, respectively.

To combine the data samples taken at various center-of-mass energies, eq. (4.6) is re-written as:

$$\ln \mathcal{L} = \sum_{n=1}^3 \ln \mathcal{L}_n, \quad (4.7)$$

where n denotes the data samples at $\sqrt{s} = 4.178$ GeV, 4.189–4.219 GeV, and 4.226 GeV, respectively.

4.2.1 Blatt-Weisskopf barriers

For a decay process $a \rightarrow bc$, the Blatt-Weisskopf barriers $X_L(q)$ [24] depend on the angular momentum $L = 0, 1, 2$ and the momentum q of the final-state particle b or c in the rest system of a . They are defined as:

$$\begin{aligned} X_{L=0}(q) &= 1, \\ X_{L=1}(q) &= \sqrt{\frac{z_0^2 + 1}{z^2 + 1}}, \\ X_{L=2}(q) &= \sqrt{\frac{z_0^4 + 3z_0^2 + 9}{z^4 + 3z^2 + 9}}, \end{aligned} \quad (4.8)$$

with $z_0 = q_0 R$ and $z = qR$, where R is the effective radius of the intermediate resonances. The momentum q is given by:

$$q = \sqrt{\frac{(s_a + s_b - s_c)^2}{4s_a} - s_b}, \quad (4.9)$$

where s_a, s_b and s_c refer to the squared invariant masses of particles a, b and c , respectively. The value of q_0 is that of q when $s_a = m_a^2$. The effective radius of barrier R is fixed to be 3.0 GeV^{-1} for the intermediate resonances and 5.0 GeV^{-1} for the D_s^+ meson.

4.2.2 Propagator

The relativistic Breit-Wigner (RBW) function is used as the propagator for the resonances $a_1(1260)^+$ and ϕ . Their masses and widths are fixed to the PDG values [1], as listed in table 4.

The RBW function is given by

$$P(m) = \frac{1}{(m_0^2 - m^2) - im_0\Gamma(m)}, \quad (4.10)$$

where $m = \sqrt{E^2 - p^2}$, m_0 is the nominal mass of the intermediate resonance, and $\Gamma(m)$ is given by:

$$\Gamma(m) = \Gamma_0 \left(\frac{q}{q_0}\right)^{2L+1} \left(\frac{m_0}{m}\right) \left(\frac{X_L(q)}{X_L(q_0)}\right)^2, \quad (4.11)$$

Resonance	Mass (MeV/c ²)	Width (MeV)
$a_1(1260)^+$	1230±40	420±50
ϕ	1019.461±0.016	4.249±0.013
ρ	775.26±0.23	147.4±0.8

Table 4. The quoted masses and widths of intermediate resonances [1].

where Γ_0 is the width of the intermediate resonance.

The ρ^0 meson is parameterised with the Gounaris-Sakurai (GS) line shape [25], which is given by:

$$P_{\text{GS}}(m) = \frac{1 + d \frac{\Gamma_0}{m_0}}{(m_0^2 - m^2) + f(m) - im_0\Gamma(m)}, \quad (4.12)$$

where:

$$f(m) = \Gamma_0 \frac{m_0^2}{q_0^3} \left[q^2(h(m) - h(m_0)) + (m_0^2 - m^2)q_0^2 \frac{dh}{d(m^2)} \Big|_{m^2=m_0^2} \right], \quad (4.13)$$

and the function $h(m)$ is defined as:

$$h(m) = \frac{2}{\pi} \frac{q}{m} \ln \left(\frac{m + 2q}{2m_\pi} \right), \quad (4.14)$$

with:

$$\frac{dh}{d(m^2)} \Big|_{m^2=m_0^2} = h(m_0)[(8q_0^2)^{-1} - (2m_0^2)^{-1}] + (2\pi m_0^2)^{-1}. \quad (4.15)$$

The normalization condition at $P_{\text{GS}}(0)$ fixes the parameter $d = \frac{f(0)}{\Gamma_0 m_0}$, which results in:

$$d = \frac{3}{\pi} \frac{m_\pi^2}{q_0^2} \ln \left(\frac{m_0 + 2q_0}{2m_\pi} \right) + \frac{m_0}{2\pi q_0} - \frac{m_\pi^2 m_0}{\pi q_0^3}. \quad (4.16)$$

4.2.3 Spin factors

Due to the limited PHSP available in the decay, we only consider the states with angular momenta up to 2. As discussed in [26], we define the spin projection operator for a process $a \rightarrow bc$, $P_{\mu_1 \dots \mu_S \nu_1 \dots \nu_S}^{(S)}$ as:

$$P_{\mu\nu}^{(1)} = -g_{\mu\nu} + \frac{p_{a\mu} p_{a\nu}}{p_a^2}, \quad (4.17)$$

$$P_{\mu_1 \mu_2 \nu_1 \nu_2}^{(2)} = \frac{1}{2} (P_{\mu_1 \nu_1}^{(1)} P_{\mu_2 \nu_2}^{(1)} + P_{\mu_1 \nu_2}^{(1)} P_{\mu_2 \nu_1}^{(1)}) - \frac{1}{3} P_{\mu_1 \mu_2}^{(1)} P_{\nu_1 \nu_2}^{(1)}. \quad (4.18)$$

The quantities p_a , p_b , and p_c are the momenta of particles a , b , and c , respectively. The covariant tensors are given by:

$$\begin{aligned} \tilde{t}_\mu^{(1)}(a) &= -P_{\mu\mu'}^{(1)}(a) r_a^{\mu'}, \\ \tilde{t}_{\mu\nu}^{(2)}(a) &= P_{\mu\nu\mu'\nu'}^{(2)}(a) r_a^{\mu'} r_a^{\nu'}. \end{aligned} \quad (4.19)$$

where $r_a = p_b - p_c$.

Eleven kinds of spin factors are listed in table 5, where the tensor describing the D_s^+ decay is denoted by \tilde{T} and the one of the a decay is denoted by \tilde{t} .

Decay chain	Spin factor
$D_s[S] \rightarrow AV_1, A[S] \rightarrow V_2P_1, V_1 \rightarrow P_2P_3, V_2 \rightarrow P_4P_5$	$P_{(1)}^{\mu\nu}(A)\tilde{t}_{(1)\mu}(V_1)\tilde{t}_{(1)\nu}(V_2)$
$D_s[S] \rightarrow AV_1, A[D] \rightarrow V_2P_1, V_1 \rightarrow P_2P_3, V_2 \rightarrow P_4P_5$	$\tilde{t}_{(2)}^{\mu\nu}(A)\tilde{t}_{(1)\mu}(V_1)\tilde{t}_{(1)\nu}(V_2)$
$D_s[P] \rightarrow AV_1, A[S] \rightarrow V_2P_1, V_1 \rightarrow P_2P_3, V_2 \rightarrow P_4P_5$	$\epsilon_{\mu\nu\lambda\sigma}p^\mu(D)\tilde{T}^{(1)\nu}(D)P_{(1)}^{\beta\lambda}(A)\tilde{t}_{(1)\beta}(V_2)\tilde{t}^{(1)\sigma}(V_1)$
$D_s[P] \rightarrow AV_1, A[D] \rightarrow V_2P_1, V_1 \rightarrow P_2P_3, V_2 \rightarrow P_4P_5$	$\epsilon_{\mu\nu\lambda\sigma}p^\mu(D)\tilde{T}^{(1)\nu}(D)\tilde{t}_{(2)}^{\beta\lambda}(A)\tilde{t}_{(1)\beta}(V_2)\tilde{t}^{(1)\sigma}(V_1)$
$D_s[D] \rightarrow AV_1, A[S] \rightarrow V_2P_1, V_1 \rightarrow P_2P_3, V_2 \rightarrow P_4P_5$	$\tilde{T}_{(2)\mu\nu}(D)P_{(1)}^{\mu\beta}(A)\tilde{t}_{(1)\beta}(V_2)\tilde{t}^{(1)\nu}(V_1)$
$D_s[D] \rightarrow AV_1, A[D] \rightarrow V_2P_1, V_1 \rightarrow P_2P_3, V_2 \rightarrow P_4P_5$	$\tilde{T}_{(2)\mu\nu}(D)\tilde{t}_{(2)}^{\mu\beta}(A)\tilde{t}_{(1)\beta}(V_2)\tilde{t}^{(1)\nu}(V_1)$
$D_s[S] \rightarrow AV, A[P] \rightarrow SP_1, V \rightarrow P_2P_3, S \rightarrow P_4P_5$	$\tilde{t}_{(1)}^\mu(A)\tilde{t}_{(1)\mu}(V)$
$D_s[P] \rightarrow AV, A[P] \rightarrow SP_1, V \rightarrow P_2P_3, S \rightarrow P_4P_5$	$\epsilon_{\mu\nu\lambda\sigma}p^\mu(D)\tilde{T}^{(1)\nu}(D)\tilde{t}_{(1)}^\lambda(A)\tilde{t}^{(1)\sigma}(V)$
$D_s[D] \rightarrow AV, A[P] \rightarrow SP_1, V \rightarrow P_2P_3, S \rightarrow P_4P_5$	$\tilde{T}_{(2)\mu\nu}(D)\tilde{t}^{(1)\mu}(A)\tilde{t}^{(1)\nu}(V)$
$D_s[P] \rightarrow AS, A[S] \rightarrow VP_1, S \rightarrow P_2P_3, V \rightarrow P_4P_5$	$\tilde{T}_{(1)\beta}(D)P_{(1)}^{\beta\nu}(A)\tilde{t}_{(1)\nu}V$
$D_s[P] \rightarrow AS, A[D] \rightarrow VP_1, S \rightarrow P_2P_3, V \rightarrow P_4P_5$	$\tilde{T}_{(1)\beta}(D)\tilde{t}_{(2)}^{\beta\nu}(A)\tilde{t}_{(1)\nu}V$

Table 5. Spin factor for each decay chain. $[S]$, $[P]$, and $[D]$ indicate the orbital angular momenta $L = 0, 1$, and 2 of the two-body final states, respectively.

4.3 Fit results

The amplitude of the $D_s^+[S] \rightarrow a_1(1260)^+\phi, a_1(1260)^+[S] \rightarrow \rho^0\pi^+, \phi \rightarrow K^-K^+$ decay is expected to have the largest contribution and it has been chosen as the reference. Thus, its magnitude and phase are fixed to 1.0 and 0.0, respectively, while the other amplitudes are left floating in the amplitude fit. The masses and widths of all the resonances are fixed to the corresponding PDG averages [1]. The background weights are fixed according to the fits shown in figure 2.

We first consider the two amplitudes $D_s^+[S] \rightarrow a_1(1260)^+\phi, a_1(1260)^+[S] \rightarrow \rho^0\pi^+, \phi \rightarrow K^-K^+$ and $D_s^+ \rightarrow (K^-K^+\pi^+\pi^-\pi^-)_{\text{NR}}$. We have tested all the possible processes including $D_s^+ \rightarrow \phi\pi^+\pi^+\pi^-$, $D_s^+ \rightarrow K_1(1270)^+\bar{K}^{*0}(892)$ and $D_s^+ \rightarrow a_1(1260)^+a_0(980)$, which are listed in appendix A, and only the amplitudes of $D_s^+[S] \rightarrow a_1(1260)^+\phi, a_1(1260)^+[S] \rightarrow \rho^0\pi^+, \phi \rightarrow K^-K^+, D_s^+[P] \rightarrow a_1(1260)^+\phi, a_1(1260)^+[S] \rightarrow \rho^0\pi^+, \phi \rightarrow K^-K^+$ and $D_s^+ \rightarrow (K^-K^+\pi^+\pi^-\pi^-)_{\text{NR}}$ have statistical significances larger than 5σ and are retained in the nominal solution. The statistical significance of each new amplitude is calculated from the change of log-likelihood taking into account the change of degrees of freedom.

The fit fractions (FFs) of the individual components (amplitudes) are calculated according to the fit results. In the calculation, a large PHSP MC sample (2.6 million events) with neither detector acceptance nor resolution included is used. Since the fit fraction does not involve efficiency, the MC sample here is used at the generator level instead of at the reconstruction level. The FF for a component or an amplitude is defined as

$$\text{FF}_n = \frac{\sum N_{\text{gen}} |\tilde{A}_n|^2}{\sum N_{\text{gen}} |\mathcal{M}|^2}, \quad (4.20)$$

where N_{gen} is the number of PHSP MC generated events, \tilde{A}_n is either the n^{th} amplitude

Amplitude	Phase	FF (%)	Significance (σ)
$D_s^+[S] \rightarrow a_1(1260)^+\phi$	0 (fixed)	$73.1 \pm 3.1 \pm 1.5$	> 10
$D_s^+[P] \rightarrow a_1(1260)^+\phi$	$1.47 \pm 0.19 \pm 0.03$	$5.0 \pm 1.7 \pm 0.7$	5.5
$D_s^+ \rightarrow a_1(1260)^+\phi$...	$78.1 \pm 2.9 \pm 1.6$...
$D_s^+ \rightarrow (K^-K^+\pi^+\pi^-\pi^-)_{\text{NR}}$	$1.99 \pm 0.12 \pm 0.17$	$21.8 \pm 2.9 \pm 0.8$	> 10

Table 6. Phases, FFs, and statistical significances for different amplitudes. The $D_s^+ \rightarrow a_1(1260)^+\phi$ is the coherent sum of the $D_s^+[S] \rightarrow a_1(1260)^+\phi$ and $D_s^+[P] \rightarrow a_1(1260)^+\phi$ amplitudes. Due to interference effects, the total FF of amplitudes is not necessarily equal to 100%. The first and the second uncertainties in the phases and FFs are statistical and systematic, respectively. In the table, the intermediate resonance $a_1(1260)^+[S]$ decays to $\rho^0\pi^+$.

($\tilde{A}_n = c_n \mathcal{A}_n$) or the n^{th} component of a coherent sum of amplitudes ($\tilde{A}_n = \sum c_{n,i} \mathcal{A}_{n,i}$). To estimate the statistical uncertainties of the FFs, we recalculate the FFs 500 times with randomly perturbing the variables determined in our fit (by a Gaussian-distributed amount controlled by the fit uncertainty and the covariance matrix). We fit the distribution of each FF with a Gaussian function and the width is reported as the uncertainty of the FF.

The phases, FFs, and statistical significances for various amplitudes are listed in table 6. The mass projections of fit results are shown in figure 3. The cosines of helicity angles for the K^-K^+ , $\pi_1^+\pi^-$, and $\pi_2^+\pi^-$ systems are shown in figure 4. The helicity angle θ_{ij} (i is K^- , π_1^+ or π_2^+ and j is K^+ or π^-) is defined as the angle between the momentum vector of the particle i in the ij rest frame and the direction of the ij system in the D_s^+ rest frame. The assignments of systematic uncertainties are discussed in the next section.

4.4 Systematic uncertainties for amplitude analysis

The systematic uncertainties for the amplitude analysis are summarised in table 7, with their assignments described below.

- (i) Resonance parameters. The masses and widths of $a_1(1260)$, ϕ and ρ are shifted by their corresponding uncertainties [1] given in table 4 and the largest variations are taken as the systematic uncertainties.
- (ii) R values. The systematic uncertainties associated with effective radii of barriers (R values) are estimated by repeating the fit procedure by varying the radii of the intermediate states and D_s^+ meson within 1 GeV^{-1} .
- (iii) Fit bias. The uncertainty due to the fit procedure is evaluated by studying signal MC samples. An ensemble of 300 signal MC samples are generated according to the nominal results of this analysis. After applying the selection criteria, each of these samples has the same size as the data sample and is used to perform the same amplitude analysis. The pull of each parameter is defined as $\frac{\text{Out}(i) - \text{In}(i)}{\sigma_{\text{stat}(i)}}$, where i denotes the different parameters, $\text{In}(i)$ denotes the input value, $\text{Out}(i)$ is the value obtained from the fit to a signal MC sample and $\sigma_{\text{stat}(i)}$ is the corresponding statistical

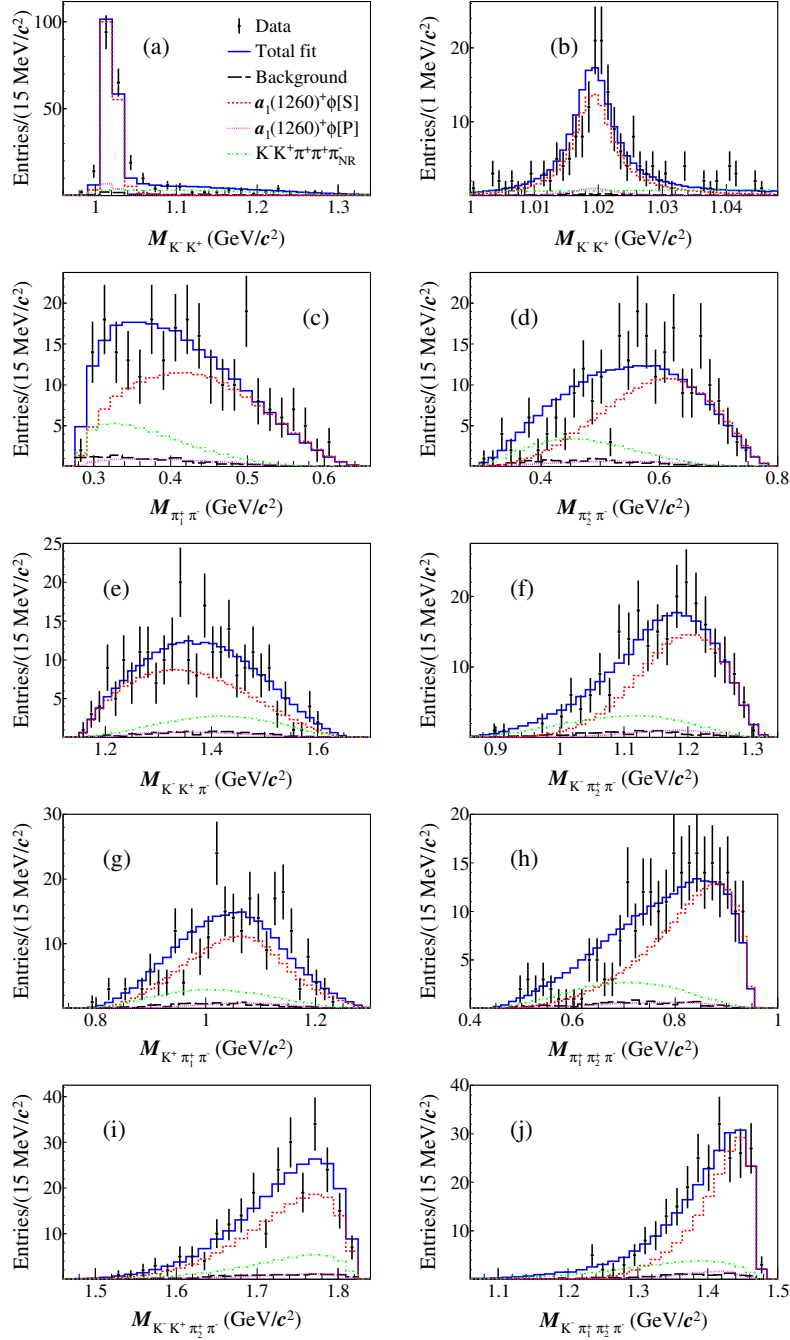


Figure 3. Mass projections from the nominal fit. The data are represented by points with error bars, and the fit results by the blue solid line. The red dashed lines are the contribution of $D_s^+[S] \rightarrow a_1(1260)^+\phi$, the magenta dotted lines are the contribution of $D_s^+[P] \rightarrow a_1(1260)^+\phi$, the green dash-dotted lines are the contribution of $D_s^+ \rightarrow (K^-K^+\pi^+\pi^+\pi^-)_{\text{NR}}$, and the black long dashed lines illustrate the background estimated from the inclusive MC samples. The plot (b) indicates the zoom of the ϕ mass region.

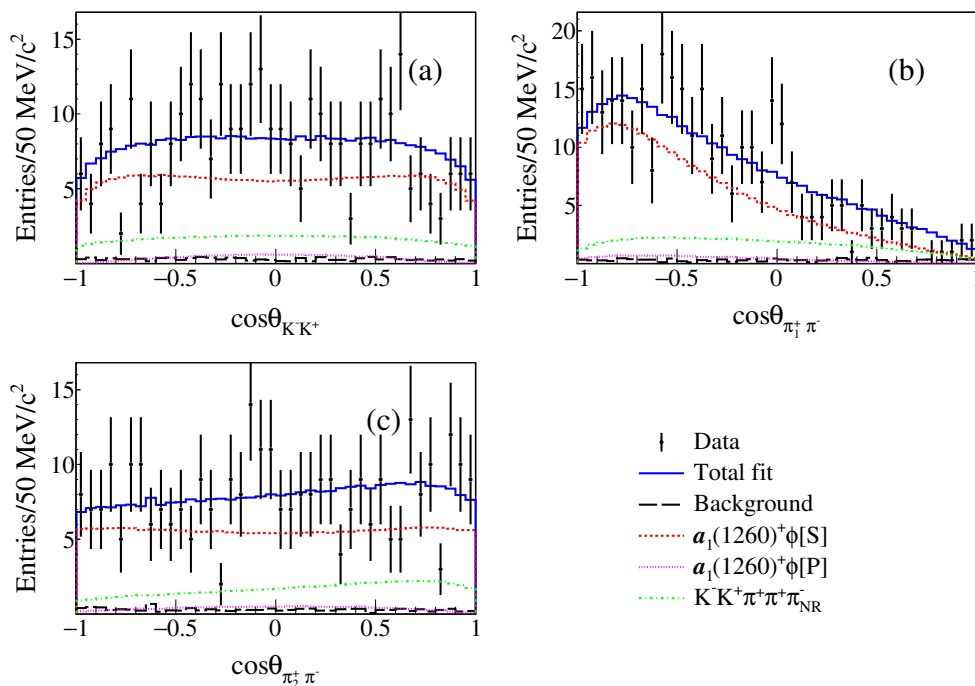


Figure 4. The cosines of helicity angles projections of fit results for the (a) K^-K^+ , (b) $\pi_1^+\pi^-$, and (c) $\pi_2^+\pi^-$ systems at $\sqrt{s} = 4.178\text{--}4.226$ GeV. The data are represented by points with error bars, and the fit results by the blue solid line. The red dashed lines are the contribution of $D_s^+[S] \rightarrow a_1(1260)^+\phi$, the magenta dotted lines are the contribution of $D_s^+[P] \rightarrow a_1(1260)^+\phi$, the green dash-dotted lines are the contribution of $D_s^+ \rightarrow (K^-K^+\pi^+\pi^-)_{\text{NR}}$, and the black long dashed lines illustrate the background estimated from the inclusive MC samples.

uncertainty. For each parameter, 300 pull values are obtained and the deviations of their average from zero are considered as the systematic uncertainty.

- (iv) Background estimation. The background is determined by the inclusive MC samples; the fractions of background events are increased or decreased by one corresponding statistical uncertainties, and the largest differences from the nominal results are considered as the uncertainties.
- (v) Lineshape of the ρ meson. An alternative lineshape parameterization with RBW instead of GS is used, and differences are included inside the uncertainties.
- (vi) Lineshape of the $a_1^+(1260)$ meson. The $\Gamma(m)$ of $a_1^+(1260)$ propagator is replaced by the decay width for the decay $a_1^+(1260) \rightarrow \pi\pi\pi$, which is calculated by the transition amplitude squared over the 3-body PHSP [27],

$$\Gamma_{a_1^+(1260) \rightarrow \pi\pi\pi}(s) = \frac{1}{2\sqrt{s}} \int |A_{a_1^+(1260) \rightarrow \pi\pi\pi}|^2 d\Phi_3, \quad (4.21)$$

where $s \equiv m^2$, and the amplitude A is parameterised similarly to the five-body amplitude in eq. (4.1). Changes of the results with respect to the nominal one are taken as the systematic uncertainties.

Amplitudes		Source						Total
		i	ii	iii	iv	v	vi	
$D_s^+[S] \rightarrow a_1(1260)^+\phi, a_1^+[S] \rightarrow \rho\pi^+$	FF	0.17	0.14	0.18	0.40	0.00	0.06	0.49
$D_s^+[P] \rightarrow a_1(1260)^+\phi, a_1^+[S] \rightarrow \rho\pi^+$	Φ	0.02	0.14	0.06	0.01	0.06	0.07	0.18
	FF	0.05	0.07	0.12	0.40	0.02	0.06	0.43
$D_s^+ \rightarrow a_1(1260)^+\phi$	FF	0.17	0.15	0.20	0.44	0.02	0.07	0.54
$D_s^+ \rightarrow (K^-K^+\pi^+\pi^+\pi^-)_{\text{NR}}$	Φ	0.33	0.23	0.08	0.04	0.04	1.34	1.40
	FF	0.04	0.10	0.15	0.20	0.01	0.10	0.29

Table 7. Systematic uncertainties on the phases and FFs for various amplitudes in units of the corresponding statistical uncertainties. The sources are: (i) the fixed parameters in the amplitudes, (ii) the R values, (iii) fit bias, (iv) background, and (v) lineshape of the ρ meson. (vi) lineshape of the $a_1^+(1260)$ meson.

(vii) Experimental effects. The PID and tracking efficiencies are studied using control samples of $e^+e^- \rightarrow K^+K^-K^+K^-$, $e^+e^- \rightarrow K^+K^-\pi^+\pi^-$, $e^+e^- \rightarrow K^+K^-\pi^+\pi^-\pi^0$, $e^+e^- \rightarrow \pi^+\pi^-\pi^+\pi^-$, and $e^+e^- \rightarrow \pi^+\pi^-\pi^+\pi^-\pi^0$ decays. The systematic uncertainties related to the efficiency difference between MC simulation and data caused by tracking and PID, reflected in the γ_ϵ in eq. (4.5), are evaluated by performing alternative fits varying tracking and PID efficiencies according to their uncertainties. The differences from the nominal results are so tiny that the related systematic uncertainties are neglected.

5 Branching fraction measurement

In addition to the selection criteria for final-state particles described in section 3, for the branching fraction measurement all the pions are subjected to an additional momentum cut $p(\pi) > 100 \text{ MeV}/c$, to remove soft pions from D^{*+} decays. The additional selection criteria in section 4.1 are not applied in the branching fraction measurement. For multiple ST candidates, the candidate with M_{rec} closest to the known mass of D_s^{*+} [1] is chosen as the best candidate. The distributions of the number of multiple ST candidate show good consistency of data and simulated samples for the M_{rec} used in this analysis. Besides the tag modes shown in table 3 in the amplitude analysis, we add another two tag modes: $D_s^- \rightarrow \pi^-\pi^-\pi^+$ and $D_s^- \rightarrow K^-\pi^-\pi^+$. The M_{tag} windows are [1.952, 1.982] and [1.953, 1.986] GeV/c^2 , respectively. The yields for various tag modes are listed in table 8, and they are obtained by fitting the corresponding M_{tag} distributions. To prevent an event being double counted in the $D_s^- \rightarrow K_S^0K^-$ and $D_s^- \rightarrow K^-\pi^+\pi^-$ selections, the value of $M_{\pi^+\pi^-}$ is required to be outside of the mass range [0.487, 0.511] GeV/c^2 for the $D_s^- \rightarrow K^-\pi^+\pi^-$ decay. As an example, the fits to the data sample at $\sqrt{s} = 4.178 \text{ GeV}$ are shown in figure 5. In the fits, the signal is modeled by a MC-simulated shape convolved with a Gaussian function to take into account the data-MC difference. The background is described by

Tag mode	(I) N_{ST}	(II) N_{ST}	(III) N_{ST}
$D_s^- \rightarrow K_S^0 K^-$	31941 ± 312	18559 ± 261	6582 ± 160
$D_s^- \rightarrow K^+ K^- \pi^-$	137240 ± 614	81286 ± 505	28439 ± 327
$D_s^- \rightarrow K_S^0 K^- \pi^0$	11385 ± 529	6832 ± 457	2227 ± 220
$D_s^- \rightarrow K^+ K^- \pi^- \pi^0$	39306 ± 799	23311 ± 659	7785 ± 453
$D_s^- \rightarrow K_S^0 K^- \pi^- \pi^+$	8093 ± 326	5269 ± 282	1662 ± 217
$D_s^- \rightarrow K_S^0 K^+ \pi^- \pi^-$	15719 ± 289	8948 ± 231	3263 ± 172
$D_s^- \rightarrow \pi^- \eta_{\gamma\gamma}$	17940 ± 402	10025 ± 339	3725 ± 252
$D_s^- \rightarrow \pi^- \pi^- \pi^+$	37977 ± 859	21909 ± 776	7511 ± 393
$D_s^- \rightarrow \pi^- \eta'$	7759 ± 141	4428 ± 111	1648 ± 74
$D_s^- \rightarrow K^- \pi^+ \pi^-$	17423 ± 666	10175 ± 448	4984 ± 458

Table 8. The ST yields for the samples collected at $\sqrt{s} =$ (I) 4.178 GeV, (II) 4.199–4.219 GeV, and (III) 4.226 GeV. The uncertainties are statistical.

a second-order Chebyshev polynomial. For the tag mode $D_s^- \rightarrow K_S^0 K^-$, there are some peaking backgrounds coming from $D^- \rightarrow K_S^0 \pi^-$. The shape of this background is taken from the inclusive MC samples and added to the fit leaving its yield floating. For the tag mode $D_s^- \rightarrow \pi^- \eta'$, there is the peaking background coming from $D_s^- \rightarrow \eta \pi^+ \pi^- \pi^-$. The shape and yield of this background are taken from the inclusive MC samples and added to the fit.

Once a tag mode is identified, we search for the signal decay $D_s^+ \rightarrow K^- K^+ \pi^+ \pi^+ \pi^-$ at the recoiling side. In the case of multiple candidates, the DT candidate with the average mass, $(M_{\text{sig}} + M_{\text{tag}})/2$, closest to the D_s^\pm nominal mass is retained. For all ST modes, we find a mean of 1.0% (0.3%) of events in data (inclusive MC) contain multiple D_s^+ signal candidates. Therefore, the effect due to the multiple signal candidates is negligible.

To measure the BF, we start from the following equations for one ST mode:

$$N_{\text{tag}}^{\text{ST}} = 2N_{D_s^+ D_s^-} \mathcal{B}_{\text{tag}} \epsilon_{\text{tag}}^{\text{ST}}, \quad (5.1)$$

$$N_{\text{tag,sig}}^{\text{DT}} = 2N_{D_s^+ D_s^-} \mathcal{B}_{\text{tag}} \mathcal{B}_{\text{sig}} \epsilon_{\text{tag,sig}}^{\text{DT}}, \quad (5.2)$$

where $N_{\text{tag}}^{\text{ST}}$ is the ST yield for the tag mode, $N_{\text{tag,sig}}^{\text{DT}}$ is the DT yield, $N_{D_s^+ D_s^-}$ is the total number of $D_s^{*\pm} D_s^\mp$ pairs produced in the $e^+ e^-$ collisions, \mathcal{B}_{tag} and \mathcal{B}_{sig} are the BFs of the tag and signal modes, respectively, $\epsilon_{\text{tag}}^{\text{ST}}$ is the ST efficiency to reconstruct the tag mode and $\epsilon_{\text{tag,sig}}^{\text{DT}}$ is the DT efficiency to reconstruct both the tag and signal decay modes. In the case of more than one tag mode and sample group,

$$N_{\text{total}}^{\text{DT}} = \sum_{\alpha,i} N_{\alpha,\text{sig},i}^{\text{DT}} = \mathcal{B}_{\text{sig}} \sum_{\alpha,i} 2N_{D_s^+ D_s^-}^i \mathcal{B}_{\alpha} \epsilon_{\alpha,\text{sig},i}^{\text{DT}}, \quad (5.3)$$

where α represents the tag modes in the i^{th} sample group. We isolate \mathcal{B}_{sig} by using eq. (5.1):

$$\mathcal{B}_{\text{sig}} = \frac{N_{\text{total}}^{\text{DT}}}{\sum_{\alpha,i} N_{\alpha,i}^{\text{ST}} \epsilon_{\alpha,\text{sig},i}^{\text{DT}} / \epsilon_{\alpha,i}^{\text{ST}}}, \quad (5.4)$$

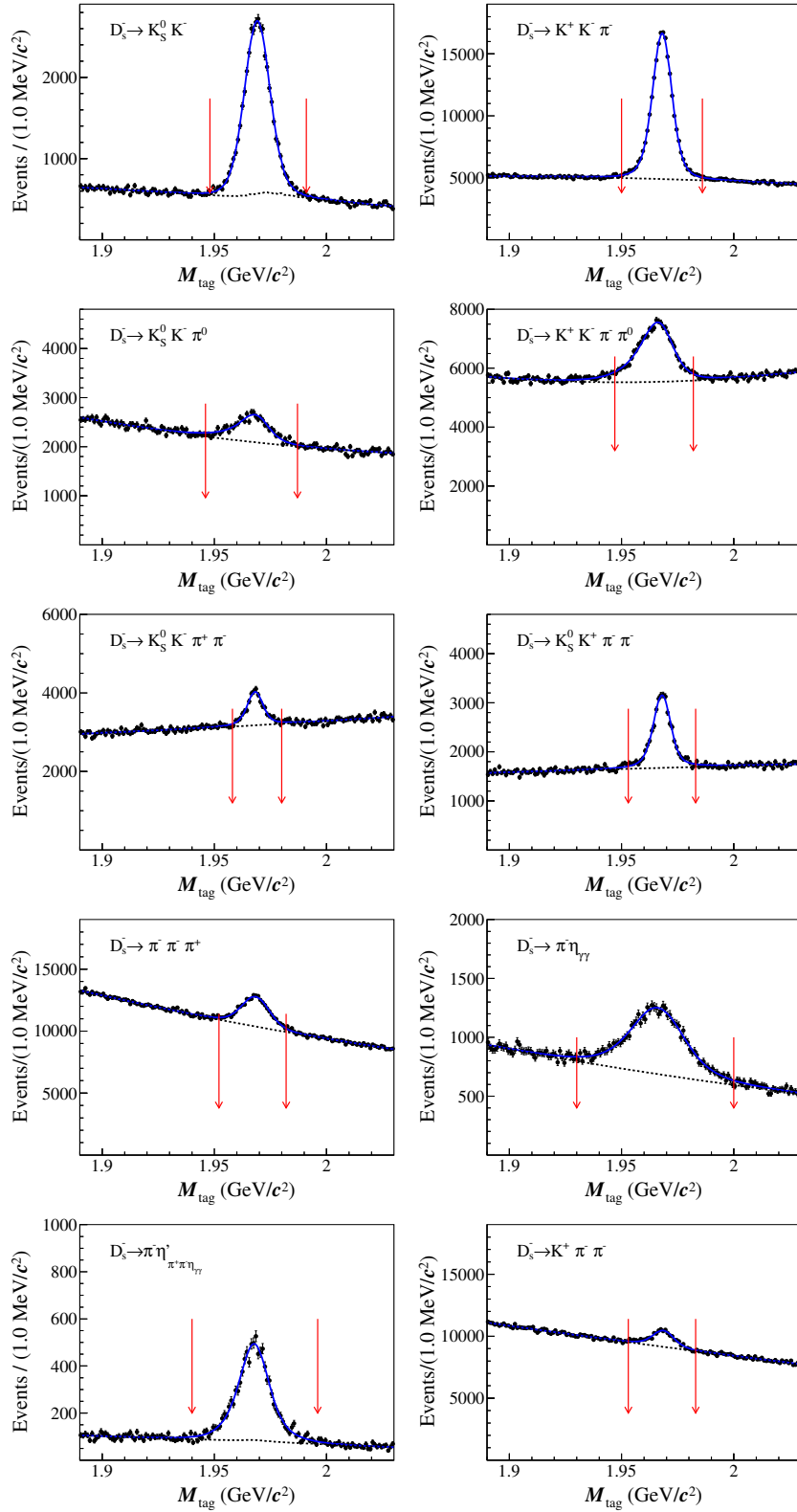


Figure 5. Fits to the M_{tag} distributions of the ST candidates from the data sample at $\sqrt{s} = 4.178$ GeV. The points with error bars are data, the blue solid lines are the total fits, and the black dashed lines are background. The pairs of red arrows denote the signal regions.

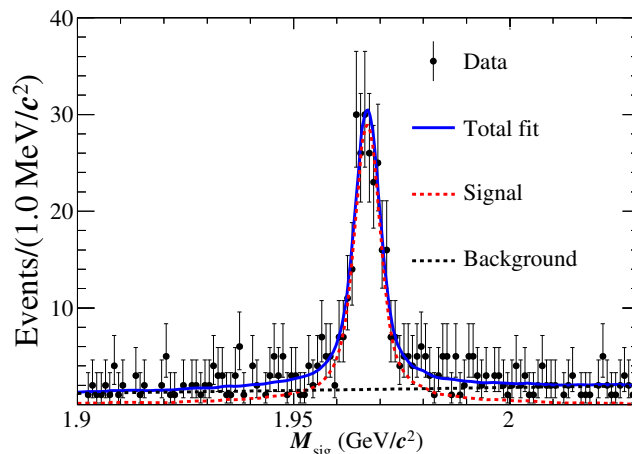


Figure 6. Fit to the M_{sig} distribution of the DT candidates from the combined data samples at $\sqrt{s} = 4.178\text{--}4.226$ GeV. The data are represented by points with error bars, the total fit by the blue solid line, and the fitted signal and the fitted background by the red dotted and the black dashed lines, respectively.

where $N_{\alpha,i}^{\text{ST}}$ and $\epsilon_{\alpha,i}^{\text{ST}}$ are obtained from the data and inclusive MC samples, respectively. We use the same ST selection criteria and fitting strategy as those used in data analysis to analyse the inclusive MC samples, and extract the number of observed ST events from fitting the M_{tag} distribution. The ST efficiency is computed as the ratio of the number of observed ST events and the number of generated ST events in the inclusive MC samples. The ST efficiency includes the mass requirement as shown in figure 5. And $\epsilon_{\alpha,\text{sig},i}^{\text{DT}}$ is determined with signal MC samples. The decay of $D_s^+ \rightarrow K^- K^+ \pi^+ \pi^+ \pi^-$ events is generated according to the results of the amplitude analysis.

The DT yield $N_{\text{total}}^{\text{DT}}$ is found to be 309 ± 22 from the fit to the M_{sig} distribution of the selected DT candidates, with purity $(60.4 \pm 2.8)\%$ for the data samples at $\sqrt{s} = 4.178\text{--}4.226$ GeV. The purity is the ratio of signal yield and total number of events in the whole mass spectrum. The fit result is shown in figure 6, where the signal shape is described by a MC-simulated shape convolved with a Gaussian function and the background shape is described by a linear function. Taking into account the differences in K^\pm and π^\pm tracking and PID efficiencies between data and MC simulation, we determine the BF of $D_s^+ \rightarrow K^- K^+ \pi^+ \pi^+ \pi^-$ to be $(6.60 \pm 0.47_{\text{stat.}} \pm 0.38_{\text{syst.}}) \times 10^{-3}$.

The systematic uncertainties in the BF measurement are discussed below. Most systematic uncertainties related to the efficiency for reconstructing the tag side cancel for BF measurement due to the DT technique.

- ST yield. We change the background shape from a second-order Chebychev polynomial to a third-order Chebychev polynomial, causing a 0.4% relative change of the branching fraction. The systematic uncertainty due to the modeling of the signal distribution is determined to be 0.35% by performing an alternative fit using the shape directly obtained from the simulated sample. The total ST yield of ten tag modes is 583210 ± 2403 , resulting in statistical uncertainty $\sqrt{(2403^2 - 583210)}/583210 = 0.4\%$. Here, we

only consider the statistical fluctuation related to the background of the tag side, as it is not correlated with the DT sample directly. The sum of these terms in quadrature is 0.7%.

- **Tracking and PID.** The tracking and PID efficiencies of K^\pm are studied with $e^+e^- \rightarrow K^+K^-K^+K^-$ and $e^+e^- \rightarrow K^+K^-\pi^+\pi^-(\pi^0)$ events. The data-MC efficiency ratios of K^+ (K^-) tracking and PID efficiencies, weighted by the corresponding momentum spectra from signal MC events, are 1.005 ± 0.017 (0.998 ± 0.015) and 0.983 ± 0.003 (0.983 ± 0.003), respectively. After correcting the MC efficiencies for these averaged data-MC differences, the systematic uncertainties of tracking and PID efficiencies per K^+ (K^-) are assigned as 1.7% (1.5%) and 0.3% (0.3%), respectively. The π^\pm tracking and PID efficiencies are studied with $e^+e^- \rightarrow K^+K^-\pi^+\pi^-(\pi^0)$, $e^+e^- \rightarrow \pi^+\pi^-\pi^+\pi^-$ and $e^+e^- \rightarrow \pi^+\pi^-\pi^+\pi^-\pi^0$ events. The data-MC efficiency ratios of the π^+ (π^-) tracking and PID efficiencies are 0.999 ± 0.005 (0.990 ± 0.005) and 1.004 ± 0.002 (1.004 ± 0.002), respectively, and we assign 0.5% (0.5%) and 0.2% (0.2%) as the systematic uncertainties arising from π^\pm tracking and PID, respectively. The systematic uncertainty of tracking is 4.7% which is treated linearly by summing up 1.7%, 1.5%, 0.5%, 0.5%, and 0.5%. The systematic uncertainty of PID is 1.2% which is treated linearly by summing up 0.3%, 0.3%, 0.2%, 0.2%, and 0.2%.
- **Signal shape.** The systematic uncertainty due to the signal shape is studied by repeating the fit without the convolved Gaussian function.
- **Background shape.** For the background shape of the signal D_s^+ , the MC-simulated shape is used to replace the linear function. The difference of the DT yields is taken as the systematic uncertainty.
- **MC statistics.** The uncertainty due to the limited MC statistics is obtained by $\sqrt{\sum_i (f_i \frac{\delta_{\epsilon_i}}{\epsilon_i})^2}$, where f_i is the tag yield fraction, and ϵ_i and δ_{ϵ_i} are the signal efficiency and the corresponding uncertainty of tag mode i , respectively.
- **Amplitude model.** The uncertainty from the amplitude model is estimated by varying the model parameters based on their error matrix. The distribution of 300 efficiency values resulting from this variation are fitted by a Gaussian function and the fitted resolution divided by the mean value is taken as uncertainty.

All of the systematic uncertainties are summarised in table 9. Adding them in quadrature gives a total systematic uncertainty in the BF measurement of 5.8%.

6 Summary

An amplitude analysis of the decay $D_s^+ \rightarrow K^-K^+\pi^+\pi^-\pi^-$ has been performed for the first time. Amplitudes with statistical significances larger than 5σ are selected. The results for the FFs and phases of the different intermediate processes are listed in table 6. With the detection efficiency determined according to the results from the amplitude analysis, the BF

Source	Systematic uncertainty (%)
ST yield	0.7
Tracking	4.7
PID	1.2
Signal shape	0.6
Background shape	1.9
MC statistics	0.6
Amplitude model	2.4
Total	5.8

Table 9. Systematic uncertainties in the BF measurement.

Intermediate process	BF (10^{-3})	PDG (10^{-3})
$D_s^+[S] \rightarrow a_1(1260)^+\phi, a_1(1260)^+[S] \rightarrow \rho^0\pi^+$	$4.82 \pm 0.40 \pm 0.29$	
$D_s^+[P] \rightarrow a_1(1260)^+\phi, a_1(1260)^+[S] \rightarrow \rho^0\pi^+$	$0.34 \pm 0.11 \pm 0.05$	
$D_s^+ \rightarrow a_1(1260)^+\phi$	$5.15 \pm 0.41 \pm 0.32$	7.4 ± 1.2
$D_s^+ \rightarrow (K^-K^+\pi^+\pi^+\pi^-)_{\text{NR}}$	$1.44 \pm 0.22 \pm 0.10$	0.9 ± 0.7

Table 10. The BFs for various intermediate processes measured in this analysis and from the PDG [1], the first and second uncertainties are statistical and systematic, respectively.

for the decay $D_s^+ \rightarrow K^-K^+\pi^+\pi^+\pi^-$ is measured to be $(6.60 \pm 0.47_{\text{stat.}} \pm 0.38_{\text{syst.}}) \times 10^{-3}$, which is consistent with the PDG value of $(8.6 \pm 1.5) \times 10^{-3}$ within 1.5σ . The BFs of the intermediate processes calculated with $\mathcal{B}_i = \text{FF}_i \times \mathcal{B}(D_s^+ \rightarrow K^-K^+\pi^+\pi^+\pi^-)$ in this analysis and those world average values from the PDG [1] are listed in table 10. The precision is improved by about a factor of two compared to the world average value.

Acknowledgments

The BESIII collaboration thanks the staff of BEPCII and the IHEP computing center for their strong support. This work is supported in part by National Key Research and Development Program of China under Contracts Nos. 2020YFA0406400, 2020YFA0406300; National Natural Science Foundation of China (NSFC) under Contracts Nos. 11625523, 11635010, 11735014, 11775027, 11822506, 11835012, 11875054, 11935015, 11935016, 11935018, 11961141012, 12192260, 12192261, 12192262, 12192263, 12192264, 1219226; the Chinese Academy of Sciences (CAS) Large-Scale Scientific Facility Program; Joint Large-Scale Scientific Facility Funds of the NSFC and CAS under Contracts Nos. U1732263, U1832207, U1932108, U2032104; CAS Key Research Program of Frontier Sciences under Contracts Nos. QYZDJ-SSW-SLH003, QYZDJ-SSW-SLH040; 100 Talents Program of CAS; INPAC and Shanghai Key Laboratory for Particle Physics and Cosmology; ERC under Contract No. 758462; European Union Horizon 2020 research and innovation

programme under Contract No. Marie Skłodowska-Curie grant agreement No. 894790; German Research Foundation DFG under Contracts Nos. 443159800, Collaborative Research Center CRC 1044, FOR 2359, FOR 2359, GRK 214; Istituto Nazionale di Fisica Nucleare, Italy; Ministry of Development of Turkey under Contract No. DPT2006K-120470; National Science and Technology fund; Olle Engkvist Foundation under Contract No. 200-0605; STFC (United Kingdom); The Knut and Alice Wallenberg Foundation (Sweden) under Contract No. 2016.0157; The Royal Society, U.K. under Contracts Nos. DH140054, DH160214; The Swedish Research Council; U.S. Department of Energy under Contracts Nos. DE-FG02-05ER41374, DE-SC-0012069.

A All other tested amplitudes

All other tested amplitudes' significances are less than 5σ , so they are not included in nominal fit and their significances are listed in table 11.

Tested Amplitude	Significance(σ)
$D_s^+[S] \rightarrow a_1(1260)^+\phi, a_1(1260)^+[D] \rightarrow \rho\pi^+, \phi \rightarrow K^-K^+$	2.7
$D_s^+[P] \rightarrow a_1(1260)^+\phi, a_1(1260)^+[D] \rightarrow \rho\pi^+, \phi \rightarrow K^-K^+$	< 1
$D_s^+[D] \rightarrow a_1(1260)^+\phi, a_1(1260)^+[S] \rightarrow \rho\pi^+, \phi \rightarrow K^-K^+$	1.5
$D_s^+[D] \rightarrow a_1(1260)^+\phi, a_1(1260)^+[D] \rightarrow \rho\pi^+, \phi \rightarrow K^-K^+$	1.5
$D_s^+[S] \rightarrow a_1(1260)^+\phi, a_1(1260)^+[P] \rightarrow f_0(500)\pi^+, \phi \rightarrow K^-K^+$	< 1
$D_s^+[P] \rightarrow a_1(1260)^+\phi, a_1(1260)^+[P] \rightarrow f_0(500)\pi^+, \phi \rightarrow K^-K^+$	< 1
$D_s^+[D] \rightarrow a_1(1260)^+\phi, a_1(1260)^+[P] \rightarrow f_0(500)\pi^+, \phi \rightarrow K^-K^+$	1.5
$D_s^+[P] \rightarrow a_1(1260)^+a_0(980), a_1(1260)^+[S] \rightarrow \rho^0\pi^+, a_0(980) \rightarrow K^-K^+$	< 1
$D_s^+[P] \rightarrow a_1(1260)^+a_0(980), a_1(1260)^+[D] \rightarrow \rho^0\pi^+, a_0(980) \rightarrow K^-K^+$	3.6
$D_s^+[S] \rightarrow K_1(1270)^+K^{*0}(\bar{892}), K_1(1270)[S] \rightarrow \rho K^+, K^{*0}(\bar{892}) \rightarrow K^-\pi^+$	< 1
$D_s^+[S] \rightarrow K_1(1270)^+K^{*0}(\bar{892}), K_1(1270)[D] \rightarrow \rho K^+, K^{*0}(\bar{892}) \rightarrow K^-\pi^+$	< 1
$D_s^+[P] \rightarrow K_1(1270)^+K^{*0}(\bar{892}), K_1(1270)[S] \rightarrow \rho K^+, K^{*0}(\bar{892}) \rightarrow K^-\pi^+$	< 1
$D_s^+[P] \rightarrow K_1(1270)^+K^{*0}(\bar{892}), K_1(1270)[D] \rightarrow \rho K^+, K^{*0}(\bar{892}) \rightarrow K^-\pi^+$	< 1
$D_s^+[D] \rightarrow K_1(1270)^+K^{*0}(\bar{892}), K_1(1270)[S] \rightarrow \rho K^+, K^{*0}(\bar{892}) \rightarrow K^-\pi^+$	1.5
$D_s^+[D] \rightarrow K_1(1270)^+K^{*0}(\bar{892}), K_1(1270)[D] \rightarrow \rho K^+, K^{*0}(\bar{892}) \rightarrow K^-\pi^+$	1.5
$D_s^+[S] \rightarrow \pi^+\pi^+\pi^-\phi, \phi \rightarrow K^-K^+$	< 1

Table 11. Tested amplitudes, but not included in the nominal fit.

Open Access. This article is distributed under the terms of the Creative Commons Attribution License ([CC-BY 4.0](https://creativecommons.org/licenses/by/4.0/)), which permits any use, distribution and reproduction in any medium, provided the original author(s) and source are credited. SCOAP³ supports the goals of the International Year of Basic Sciences for Sustainable Development.

References

- [1] PARTICLE DATA GROUP collaboration, *Review of Particle Physics*, *PTEP* **2020** (2020) 083C01 [INSPIRE].
- [2] H.J. Lipkin, *Systematics of large axial vector meson production in heavy flavor weak decays*, *Phys. Lett. B* **515** (2001) 81 [hep-ph/0011228] [INSPIRE].
- [3] HFLAV collaboration, *Averages of b-hadron, c-hadron, and τ -lepton properties as of summer 2016*, *Eur. Phys. J. C* **77** (2017) 895 [arXiv:1612.07233] [INSPIRE].
- [4] LHCb collaboration, *Measurement of the ratio of the $B^0 \rightarrow D^{*-}\tau^+\nu_\tau$ and $B^0 \rightarrow D^{*-}\mu^+\nu_\mu$ branching fractions using three-prong τ -lepton decays*, *Phys. Rev. Lett.* **120** (2018) 171802 [arXiv:1708.08856] [INSPIRE].
- [5] LHCb collaboration, *Test of Lepton Flavor Universality by the measurement of the $B^0 \rightarrow D^{*-}\tau^+\nu_\tau$ branching fraction using three-prong τ decays*, *Phys. Rev. D* **97** (2018) 072013 [arXiv:1711.02505] [INSPIRE].
- [6] E687 collaboration, *Study of charged hadronic five-body decays of the D^+ and D_s^+ mesons*, *Phys. Lett. B* **401** (1997) 131 [INSPIRE].
- [7] FOCUS collaboration, *Study of Hadronic Five-Body Decays of Charmed Mesons*, *Phys. Lett. B* **561** (2003) 225 [hep-ex/0211056] [INSPIRE].
- [8] BESIII collaboration, *Design and Construction of the BESIII Detector*, *Nucl. Instrum. Meth. A* **614** (2010) 345 [arXiv:0911.4960] [INSPIRE].
- [9] C. Yu et al., *BEPCII performance and beam dynamics studies on luminosity*, in *Proc. of International Particle Accelerator Conference (IPAC'16)*, Busan, Korea, 8–13 May 2016, no. 7 in International Particle Accelerator Conference, Geneva, Switzerland, pp. 1014–1018, JACoW (2016) [DOI].
- [10] BESIII collaboration, *Future Physics Programme of BESIII*, *Chin. Phys. C* **44** (2020) 040001 [arXiv:1912.05983] [INSPIRE].
- [11] X. Li et al., *Study of MRPC technology for BESIII endcap-TOF upgrade*, *Radiat. Detect. Technol. Methods* **1** (2017) 13.
- [12] Y.-X. Guo et al., *The study of time calibration for upgraded end cap TOF of BESIII*, *Radiat. Detect. Technol. Methods* **1** (2017) 15.
- [13] P. Cao et al., *Design and construction of the new BESIII endcap Time-of-Flight system with MRPC technology*, *Nucl. Instrum. Meth. A* **953** (2020) 163053.
- [14] BESIII collaboration, *Measurement of the integrated luminosities at BESIII for data samples at collision energies around 4 GeV*, in preparation.
- [15] GEANT4 collaboration, *GEANT4 — a simulation toolkit*, *Nucl. Instrum. Meth. A* **506** (2003) 250 [INSPIRE].
- [16] S. Jadach, B.F.L. Ward and Z. Was, *Coherent exclusive exponentiation for precision Monte Carlo calculations*, *Phys. Rev. D* **63** (2001) 113009 [hep-ph/0006359] [INSPIRE].
- [17] S. Jadach, B.F.L. Ward and Z. Was, *The Precision Monte Carlo event generator KK for two fermion final states in e^+e^- collisions*, *Comput. Phys. Commun.* **130** (2000) 260 [hep-ph/9912214] [INSPIRE].

- [18] D.J. Lange, *The EvtGen particle decay simulation package*, *Nucl. Instrum. Meth. A* **462** (2001) 152 [INSPIRE].
- [19] R.-G. Ping, *Event generators at BESIII*, *Chin. Phys. C* **32** (2008) 599 [INSPIRE].
- [20] J.C. Chen, G.S. Huang, X.R. Qi, D.H. Zhang and Y.S. Zhu, *Event generator for J/ψ and $\psi(2S)$ decay*, *Phys. Rev. D* **62** (2000) 034003 [INSPIRE].
- [21] R.-L. Yang, R.-G. Ping and H. Chen, *Tuning and Validation of the Lundcharm Model with J/ψ Decays*, *Chin. Phys. Lett.* **31** (2014) 061301 [INSPIRE].
- [22] E. Richter-Was, *QED bremsstrahlung in semileptonic B and leptonic tau decays*, *Phys. Lett. B* **303** (1993) 163 [INSPIRE].
- [23] MARK-III collaboration, *Direct Measurements of Charmed d Meson Hadronic Branching Fractions*, *Phys. Rev. Lett.* **56** (1986) 2140 [INSPIRE].
- [24] BESIII collaboration, *Amplitude analysis and branching fraction measurement of $D_s^+ \rightarrow K^+ K^- \pi^+$* , *Phys. Rev. D* **104** (2021) 012016 [arXiv:2011.08041] [INSPIRE].
- [25] G.J. Gounaris and J.J. Sakurai, *Finite width corrections to the vector meson dominance prediction for $\rho \rightarrow e^+ e^-$* , *Phys. Rev. Lett.* **21** (1968) 244 [INSPIRE].
- [26] B.S. Zou and D.V. Bugg, *Covariant tensor formalism for partial wave analyses of psi decay to mesons*, *Eur. Phys. J. A* **16** (2003) 537 [hep-ph/0211457] [INSPIRE].
- [27] P. d'Argent et al., *Amplitude Analyses of $D^0 \rightarrow \pi^+ \pi^- \pi^+ \pi^-$ and $D^0 \rightarrow K^+ K^- \pi^+ \pi^-$ Decays*, *JHEP* **05** (2017) 143 [arXiv:1703.08505] [INSPIRE].

The BESIII collaboration

M. Ablikim¹, M.N. Achasov^{10,b}, P. Adlarson⁶⁷, S. Ahmed¹⁵, M. Albrecht⁴, R. Aliberti²⁸, A. Amoroso^{66A,66C}, M.R. An³², Q. An^{63,49}, X.H. Bai⁵⁷, Y. Bai⁴⁸, O. Bakina²⁹, R. Baldini Ferroli^{23A}, I. Balossino^{24A}, Y. Ban^{38,i}, K. Begzsuren²⁶, N. Berger²⁸, M. Bertani^{23A}, D. Bettoni^{24A}, F. Bianchi^{66A,66C}, J. Bloms⁶⁰, A. Bortone^{66A,66C}, I. Boyko²⁹, R.A. Briere⁵, H. Cai⁶⁸, X. Cai^{1,49}, A. Calcaterra^{23A}, G.F. Cao^{1,54}, N. Cao^{1,54}, S.A. Cetin^{53A}, J.F. Chang^{1,49}, W.L. Chang^{1,54}, G. Chelkov^{29,a}, D.Y. Chen⁶, G. Chen¹, H.S. Chen^{1,54}, M.L. Chen^{1,49}, S.J. Chen³⁵, X.R. Chen²⁵, Y.B. Chen^{1,49}, Z. J. Chen^{20,j}, W.S. Cheng^{66C}, G. Cibinetto^{24A}, F. Cossio^{66C}, X.F. Cui³⁶, H.L. Dai^{1,49}, X.C. Dai^{1,54}, A. Dbeyssi¹⁵, R. E. de Boer⁴, D. Dedovich²⁹, Z.Y. Deng¹, A. Denig²⁸, I. Denysenko²⁹, M. Destefanis^{66A,66C}, F. De Mori^{66A,66C}, Y. Ding³³, C. Dong³⁶, J. Dong^{1,49}, L.Y. Dong^{1,54}, M.Y. Dong^{1,49,54}, X. Dong⁶⁸, S.X. Du⁷¹, Y.L. Fan⁶⁸, J. Fang^{1,49}, S.S. Fang^{1,54}, Y. Fang¹, R. Farinelli^{24A}, L. Fava^{66B,66C}, F. Feldbauer⁴, G. Felici^{23A}, C.Q. Feng^{63,49}, J.H. Feng⁵⁰, M. Fritsch⁴, C.D. Fu¹, Y. Gao^{38,i}, Y. Gao⁶⁴, Y. Gao^{63,49}, Y.G. Gao⁶, I. Garzia^{24A,24B}, P.T. Ge⁶⁸, C. Geng⁵⁰, E.M. Gersabeck⁵⁸, A. Gilman⁶¹, K. Goetzen¹¹, L. Gong³³, W.X. Gong^{1,49}, W. Gradl²⁸, M. Greco^{66A,66C}, L.M. Gu³⁵, M.H. Gu^{1,49}, S. Gu², Y.T. Gu¹³, C. Y Guan^{1,54}, A.Q. Guo²², L.B. Guo³⁴, R.P. Guo⁴⁰, Y.P. Guo^{9,g}, A. Guskov^{29,a}, T.T. Han⁴¹, W.Y. Han³², X.Q. Hao¹⁶, F.A. Harris⁵⁶, K.L. He^{1,54}, F.H. Heinsius⁴, C.H. Heinz²⁸, T. Held⁴, Y.K. Heng^{1,49,54}, C. Herold⁵¹, M. Himmelreich^{11,e}, T. Holtmann⁴, G.Y. Hou^{1,54}, Y.R. Hou⁵⁴, Z.L. Hou¹, H.M. Hu^{1,54}, J.F. Hu^{47,k}, T. Hu^{1,49,54}, Y. Hu¹, G.S. Huang^{63,49}, L.Q. Huang⁶⁴, X.T. Huang⁴¹, Y.P. Huang¹, Z. Huang^{38,i}, T. Hussain⁶⁵, N. Hüsken^{22,28}, W. Ikegami Andersson⁶⁷, W. Imoehl²², M. Irshad^{63,49}, S. Jaeger⁴, S. Janchiv²⁶, Q. Ji¹, Q.P. Ji¹⁶, X.B. Ji^{1,54}, X.L. Ji^{1,49}, Y.Y. Ji⁴¹, H.B. Jiang⁴¹, X.S. Jiang^{1,49,54}, J.B. Jiao⁴¹, Z. Jiao¹⁸, S. Jin³⁵, Y. Jin⁵⁷, M.Q. Jing^{1,54}, T. Johansson⁶⁷, N. Kalantar-Nayestanaki⁵⁵, X.S. Kang³³, R. Kappert⁵⁵, M. Kavatsyuk⁵⁵, B.C. Ke^{71,1}, I.K. Keshk⁴, A. Khoukaz⁶⁰, P. Kiese²⁸, R. Kiuchi¹, R. Kliemt¹¹, L. Koch³⁰, O.B. Kolcu^{53A,d}, B. Kopf⁴, M. Kuemmel⁴, M. Kuessner⁴, A. Kupsc⁶⁷, M. G. Kurth^{1,54}, W. Kühn³⁰, J.J. Lane⁵⁸, J.S. Lange³⁰, P. Larin¹⁵, A. Lavania²¹, L. Lavezzi^{66A,66C}, Z.H. Lei^{63,49}, H. Leithoff²⁸, M. Lellmann²⁸, T. Lenz²⁸, C. Li³⁹, C.H. Li³², Cheng Li^{63,49}, D.M. Li⁷¹, F. Li^{1,49}, G. Li¹, H. Li^{63,49}, H. Li⁴³, H.B. Li^{1,54}, H.J. Li¹⁶, J.L. Li⁴¹, J.Q. Li⁴, J.S. Li⁵⁰, Ke Li¹, L.K. Li¹, Lei Li³, P.R. Li^{31,l,m}, S.Y. Li⁵², W.D. Li^{1,54}, W.G. Li¹, X.H. Li^{63,49}, X.L. Li⁴¹, Xiaoyu Li^{1,54}, Z.Y. Li⁵⁰, H. Liang^{63,49}, H. Liang^{1,54}, H. Liang²⁷, Y.F. Liang⁴⁵, Y.T. Liang²⁵, G.R. Liao¹², L.Z. Liao^{1,54}, J. Libby²¹, C.X. Lin⁵⁰, B.J. Liu¹, C.X. Liu¹, D. Liu^{63,49}, F.H. Liu⁴⁴, Fang Liu¹, Feng Liu⁶, H.B. Liu¹³, H.M. Liu^{1,54}, Huanhuan Liu¹, Huihui Liu¹⁷, J.B. Liu^{63,49}, J.L. Liu⁶⁴, J.Y. Liu^{1,54}, K. Liu¹, K.Y. Liu³³, L. Liu^{63,49}, M.H. Liu^{9,g}, P.L. Liu¹, Q. Liu⁶⁸, Q. Liu⁵⁴, S.B. Liu^{63,49}, Shuai Liu⁴⁶, T. Liu^{1,54}, W.M. Liu^{63,49}, X. Liu^{31,l,m}, Y. Liu^{31,l,m}, Y.B. Liu³⁶, Z.A. Liu^{1,49,54}, Z.Q. Liu⁴¹, X.C. Lou^{1,49,54}, F.X. Lu⁵⁰, H.J. Lu¹⁸, J.D. Lu^{1,54}, J.G. Lu^{1,49}, X.L. Lu¹, Y. Lu¹, Y.P. Lu^{1,49}, C.L. Luo³⁴, M.X. Luo⁷⁰, P.W. Luo⁵⁰, T. Luo^{9,g}, X.L. Luo^{1,49}, X.R. Lyu⁵⁴, F.C. Ma³³, H.L. Ma¹, L.L. Ma⁴¹, M.M. Ma^{1,54}, Q.M. Ma¹, R.Q. Ma^{1,54}, R.T. Ma⁵⁴, X.X. Ma^{1,54}, X.Y. Ma^{1,49}, F.E. Maas¹⁵, M. Maggiora^{66A,66C}, S. Maldaner⁴, S. Malde⁶¹, Q.A. Malik⁶⁵, A. Mangoni^{23B}, Y.J. Mao^{38,i}, Z.P. Mao¹, S. Marcello^{66A,66C}, Z.X. Meng⁵⁷, J.G. Messchendorp⁵⁵, G. Mezzadri^{24A}, T.J. Min³⁵, R.E. Mitchell²², X.H. Mo^{1,49,54}, Y.J. Mo⁶, N. Yu. Muchnoi^{10,b}, H. Muramatsu⁵⁹, S. Nakhoul^{11,e}, Y. Nefedov²⁹, F. Nerling^{11,e}, I.B. Nikolaev^{10,b}, Z. Ning^{1,49}, S. Nisar^{8,h}, S.L. Olsen⁵⁴, Q. Ouyang^{1,49,54}, S. Pacetti^{23B,23C}, X. Pan^{9,g}, Y. Pan⁵⁸, A. Pathak¹, A. Pathak²⁷, P. Patteri^{23A}, M. Pelizaeus⁴, H.P. Peng^{63,49}, K. Peters^{11,e}, J. Pettersson⁶⁷, J.L. Ping³⁴, R.G. Ping^{1,54}, R. Poling⁵⁹, V. Prasad^{63,49}, H. Qi^{63,49}, H.R. Qi⁵², K.H. Qi²⁵, M. Qi³⁵, T.Y. Qi⁹, S. Qian^{1,49}, W.B. Qian⁵⁴, Z. Qian⁵⁰, C.F. Qiao⁵⁴, L.Q. Qin¹², X.P. Qin⁹, X.S. Qin⁴¹, Z.H. Qin^{1,49}, J.F. Qiu¹, S.Q. Qu³⁶, K.H. Rashid⁶⁵, K. Ravindran²¹, C.F. Redmer²⁸, A. Rivetti^{66C}, V. Rodin⁵⁵, M. Rolo^{66C}, G. Rong^{1,54}, Ch. Rosner¹⁵, M. Rump⁶⁰, H.S. Sang⁶³, A. Sarantsev^{29,c}, Y. Schelhaas²⁸, C. Schnier⁴,

K. Schoenning⁶⁷, M. Scodeggio^{24A,24B}, D.C. Shan⁴⁶, W. Shan¹⁹, X.Y. Shan^{63,49}, J.F. Shangguan⁴⁶, M. Shao^{63,49}, C.P. Shen⁹, H.F. Shen^{1,54}, P.X. Shen³⁶, X.Y. Shen^{1,54}, H.C. Shi^{63,49}, R.S. Shi^{1,54}, X. Shi^{1,49}, X. D Shi^{63,49}, J.J. Song⁴¹, W.M. Song^{27,1}, Y.X. Song^{38,i}, S. Sosio^{66A,66C}, S. Spataro^{66A,66C}, K.X. Su⁶⁸, P.P. Su⁴⁶, F.F. Sui⁴¹, G.X. Sun¹, H.K. Sun¹, J.F. Sun¹⁶, L. Sun⁶⁸, S.S. Sun^{1,54}, T. Sun^{1,54}, W.Y. Sun³⁴, W.Y. Sun²⁷, X Sun^{20,j}, Y.J. Sun^{63,49}, Y.K. Sun^{63,49}, Y.Z. Sun¹, Z.T. Sun¹, Y.H. Tan⁶⁸, Y.X. Tan^{63,49}, C.J. Tang⁴⁵, G.Y. Tang¹, J. Tang⁵⁰, J.X. Teng^{63,49}, V. Thoren⁶⁷, W.H. Tian⁴³, Y.T. Tian²⁵, I. Uman^{53B}, B. Wang¹, C.W. Wang³⁵, D.Y. Wang^{38,i}, H.J. Wang^{31,l,m}, H.P. Wang^{1,54}, K. Wang^{1,49}, L.L. Wang¹, M. Wang⁴¹, M.Z. Wang^{38,i}, Meng Wang^{1,54}, W. Wang⁵⁰, W.H. Wang⁶⁸, W.P. Wang^{63,49}, X. Wang^{38,i}, X.F. Wang^{31,l,m}, X.L. Wang^{9,g}, Y. Wang⁵⁰, Y. Wang^{63,49}, Y.D. Wang³⁷, Y.F. Wang^{1,49,54}, Y.Q. Wang^{1,54}, Y.Y. Wang^{31,l,m}, Z. Wang^{1,49}, Z.Y. Wang¹, Ziyi Wang⁵⁴, Zongyuan Wang^{1,54}, D.H. Wei¹², F. Weidner⁶⁰, S.P. Wen¹, D.J. White⁵⁸, U. Wiedner⁴, G. Wilkinson⁶¹, M. Wolke⁶⁷, L. Wollenberg⁴, J.F. Wu^{1,54}, L.H. Wu¹, L.J. Wu^{1,54}, X. Wu^{9,g}, Z. Wu^{1,49}, L. Xia^{63,49}, H. Xiao^{9,g}, S.Y. Xiao¹, Z.J. Xiao³⁴, X.H. Xie^{38,i}, Y.G. Xie^{1,49}, Y.H. Xie⁶, T.Y. Xing^{1,54}, G.F. Xu¹, Q.J. Xu¹⁴, W. Xu^{1,54}, X.P. Xu⁴⁶, Y.C. Xu⁵⁴, F. Yan^{9,g}, L. Yan^{9,g}, W.B. Yan^{63,49}, W.C. Yan⁷¹, Xu Yan⁴⁶, H.J. Yang^{42,f}, H.X. Yang¹, L. Yang⁴³, S.L. Yang⁵⁴, Y.X. Yang¹², Yifan Yang^{1,54}, Zhi Yang²⁵, M. Ye^{1,49}, M.H. Ye⁷, J.H. Yin¹, Z.Y. You⁵⁰, B.X. Yu^{1,49,54}, C.X. Yu³⁶, G. Yu^{1,54}, J.S. Yu^{20,j}, T. Yu⁶⁴, C.Z. Yuan^{1,54}, L. Yuan², X.Q. Yuan^{38,i}, Y. Yuan¹, Z.Y. Yuan⁵⁰, C.X. Yue³², A.A. Zafar⁶⁵, X. Zeng⁶, Y. Zeng^{20,j}, A.Q. Zhang¹, B.X. Zhang¹, Guangyi Zhang¹⁶, H. Zhang⁶³, H.H. Zhang²⁷, H.H. Zhang⁵⁰, H.Y. Zhang^{1,49}, J.J. Zhang⁴³, J.L. Zhang⁶⁹, J.Q. Zhang³⁴, J.W. Zhang^{1,49,54}, J.Y. Zhang¹, J.Z. Zhang^{1,54}, Jianyu Zhang^{1,54}, Jiawei Zhang^{1,54}, L.M. Zhang⁵², L.Q. Zhang⁵⁰, Lei Zhang³⁵, S. Zhang⁵⁰, S.F. Zhang³⁵, Shulei Zhang^{20,j}, X.D. Zhang³⁷, X.Y. Zhang⁴¹, Y. Zhang⁶¹, Y.T. Zhang⁷¹, Y.H. Zhang^{1,49}, Yan Zhang^{63,49}, Yao Zhang¹, Z.H. Zhang⁶, Z.Y. Zhang⁶⁸, G. Zhao¹, J. Zhao³², J.Y. Zhao^{1,54}, J.Z. Zhao^{1,49}, Lei Zhao^{63,49}, Ling Zhao¹, M.G. Zhao³⁶, Q. Zhao¹, S.J. Zhao⁷¹, Y.B. Zhao^{1,49}, Y.X. Zhao²⁵, Z.G. Zhao^{63,49}, A. Zhemchugov^{29,a}, B. Zheng⁶⁴, J.P. Zheng^{1,49}, Y. Zheng^{38,i}, Y.H. Zheng⁵⁴, B. Zhong³⁴, C. Zhong⁶⁴, L.P. Zhou^{1,54}, Q. Zhou^{1,54}, X. Zhou⁶⁸, X.K. Zhou⁵⁴, X.R. Zhou^{63,49}, X.Y. Zhou³², A.N. Zhu^{1,54}, J. Zhu³⁶, K. Zhu¹, K.J. Zhu^{1,49,54}, S.H. Zhu⁶², T.J. Zhu⁶⁹, W.J. Zhu^{9,g}, W.J. Zhu³⁶, X.Y. Zhu¹⁶, Y.C. Zhu^{63,49}, Z.A. Zhu^{1,54}, B.S. Zou¹ and J.H. Zou¹

¹ *Institute of High Energy Physics, Beijing 100049, People's Republic of China*

² *Beihang University, Beijing 100191, People's Republic of China*

³ *Beijing Institute of Petrochemical Technology, Beijing 102617, People's Republic of China*

⁴ *Bochum Ruhr-University, D-44780 Bochum, Germany*

⁵ *Carnegie Mellon University, Pittsburgh, Pennsylvania 15213, U.S.A.*

⁶ *Central China Normal University, Wuhan 430079, People's Republic of China*

⁷ *China Center of Advanced Science and Technology, Beijing 100190, People's Republic of China*

⁸ *COMSATS University Islamabad, Lahore Campus, Defence Road, Off Raiwind Road, 54000 Lahore, Pakistan*

⁹ *Fudan University, Shanghai 200443, People's Republic of China*

¹⁰ *G.I. Budker Institute of Nuclear Physics SB RAS (BINP), Novosibirsk 630090, Russia*

¹¹ *GSI Helmholtzcentre for Heavy Ion Research GmbH, D-64291 Darmstadt, Germany*

¹² *Guangxi Normal University, Guilin 541004, People's Republic of China*

¹³ *Guangxi University, Nanning 530004, People's Republic of China*

¹⁴ *Hangzhou Normal University, Hangzhou 310036, People's Republic of China*

¹⁵ *Helmholtz Institute Mainz, Staudinger Weg 18, D-55099 Mainz, Germany*

¹⁶ *Henan Normal University, Xinxiang 453007, People's Republic of China*

¹⁷ *Henan University of Science and Technology, Luoyang 471003, People's Republic of China*

¹⁸ *Huangshan College, Huangshan 245000, People's Republic of China*

¹⁹ *Hunan Normal University, Changsha 410081, People's Republic of China*

- ²⁰ Hunan University, Changsha 410082, People's Republic of China
- ²¹ Indian Institute of Technology Madras, Chennai 600036, India
- ²² Indiana University, Bloomington, Indiana 47405, U.S.A.
- ²³ INFN Laboratori Nazionali di Frascati, (A) INFN Laboratori Nazionali di Frascati, I-00044, Frascati, Italy; (B) INFN Sezione di Perugia, I-06100, Perugia, Italy; (C) University of Perugia, I-06100, Perugia, Italy
- ²⁴ INFN Sezione di Ferrara, (A) INFN Sezione di Ferrara, I-44122, Ferrara, Italy; (B) University of Ferrara, I-44122, Ferrara, Italy
- ²⁵ Institute of Modern Physics, Lanzhou 730000, People's Republic of China
- ²⁶ Institute of Physics and Technology, Peace Ave. 54B, Ulaanbaatar 13330, Mongolia
- ²⁷ Jilin University, Changchun 130012, People's Republic of China
- ²⁸ Johannes Gutenberg University of Mainz, Johann-Joachim-Becher-Weg 45, D-55099 Mainz, Germany
- ²⁹ Joint Institute for Nuclear Research, 141980 Dubna, Moscow region, Russia
- ³⁰ Justus-Liebig-Universitaet Giessen, II. Physikalisches Institut, Heinrich-Buff-Ring 16, D-35392 Giessen, Germany
- ³¹ Lanzhou University, Lanzhou 730000, People's Republic of China
- ³² Liaoning Normal University, Dalian 116029, People's Republic of China
- ³³ Liaoning University, Shenyang 110036, People's Republic of China
- ³⁴ Nanjing Normal University, Nanjing 210023, People's Republic of China
- ³⁵ Nanjing University, Nanjing 210093, People's Republic of China
- ³⁶ Nankai University, Tianjin 300071, People's Republic of China
- ³⁷ North China Electric Power University, Beijing 102206, People's Republic of China
- ³⁸ Peking University, Beijing 100871, People's Republic of China
- ³⁹ Qufu Normal University, Qufu 273165, People's Republic of China
- ⁴⁰ Shandong Normal University, Jinan 250014, People's Republic of China
- ⁴¹ Shandong University, Jinan 250100, People's Republic of China
- ⁴² Shanghai Jiao Tong University, Shanghai 200240, People's Republic of China
- ⁴³ Shanxi Normal University, Linfen 041004, People's Republic of China
- ⁴⁴ Shanxi University, Taiyuan 030006, People's Republic of China
- ⁴⁵ Sichuan University, Chengdu 610064, People's Republic of China
- ⁴⁶ Soochow University, Suzhou 215006, People's Republic of China
- ⁴⁷ South China Normal University, Guangzhou 510006, People's Republic of China
- ⁴⁸ Southeast University, Nanjing 211100, People's Republic of China
- ⁴⁹ State Key Laboratory of Particle Detection and Electronics, Beijing 100049, Hefei 230026, People's Republic of China
- ⁵⁰ Sun Yat-Sen University, Guangzhou 510275, People's Republic of China
- ⁵¹ Suranaree University of Technology, University Avenue 111, Nakhon Ratchasima 30000, Thailand
- ⁵² Tsinghua University, Beijing 100084, People's Republic of China
- ⁵³ Turkish Accelerator Center Particle Factory Group, (A) Istanbul Bilgi University, HEP Res. Cent., 34060 Eyup, Istanbul, Turkey; (B) Near East University, Nicosia, North Cyprus, Mersin 10, Turkey
- ⁵⁴ University of Chinese Academy of Sciences, Beijing 100049, People's Republic of China
- ⁵⁵ University of Groningen, NL-9747 AA Groningen, The Netherlands
- ⁵⁶ University of Hawaii, Honolulu, Hawaii 96822, U.S.A.
- ⁵⁷ University of Jinan, Jinan 250022, People's Republic of China
- ⁵⁸ University of Manchester, Oxford Road, Manchester, M13 9PL, United Kingdom
- ⁵⁹ University of Minnesota, Minneapolis, Minnesota 55455, U.S.A.
- ⁶⁰ University of Muenster, Wilhelm-Klemm-Str. 9, 48149 Muenster, Germany
- ⁶¹ University of Oxford, Keble Rd, Oxford, U.K. OX13RH
- ⁶² University of Science and Technology Liaoning, Anshan 114051, People's Republic of China
- ⁶³ University of Science and Technology of China, Hefei 230026, People's Republic of China
- ⁶⁴ University of South China, Hengyang 421001, People's Republic of China
- ⁶⁵ University of the Punjab, Lahore-54590, Pakistan

- ⁶⁶ *University of Turin and INFN, (A) University of Turin, I-10125, Turin, Italy; (B) University of Eastern Piedmont, I-15121, Alessandria, Italy; (C) INFN, I-10125, Turin, Italy*
- ⁶⁷ *Uppsala University, Box 516, SE-75120 Uppsala, Sweden*
- ⁶⁸ *Wuhan University, Wuhan 430072, People's Republic of China*
- ⁶⁹ *Xinyang Normal University, Xinyang 464000, People's Republic of China*
- ⁷⁰ *Zhejiang University, Hangzhou 310027, People's Republic of China*
- ⁷¹ *Zhengzhou University, Zhengzhou 450001, People's Republic of China*
- ^a *Also at the Moscow Institute of Physics and Technology, Moscow 141700, Russia*
- ^b *Also at the Novosibirsk State University, Novosibirsk, 630090, Russia*
- ^c *Also at the NRC "Kurchatov Institute", PNPI, 188300, Gatchina, Russia*
- ^d *Currently at Istanbul Arel University, 34295 Istanbul, Turkey*
- ^e *Also at Goethe University Frankfurt, 60323 Frankfurt am Main, Germany*
- ^f *Also at Key Laboratory for Particle Physics, Astrophysics and Cosmology, Ministry of Education; Shanghai Key Laboratory for Particle Physics and Cosmology; Institute of Nuclear and Particle Physics, Shanghai 200240, People's Republic of China*
- ^g *Also at Key Laboratory of Nuclear Physics and Ion-beam Application (MOE) and Institute of Modern Physics, Fudan University, Shanghai 200443, People's Republic of China*
- ^h *Also at Harvard University, Department of Physics, Cambridge, MA, 02138, U.S.A.*
- ⁱ *Also at State Key Laboratory of Nuclear Physics and Technology, Peking University, Beijing 100871, People's Republic of China*
- ^j *Also at School of Physics and Electronics, Hunan University, Changsha 410082, China*
- ^k *Also at Guangdong Provincial Key Laboratory of Nuclear Science, Institute of Quantum Matter, South China Normal University, Guangzhou 510006, China*
- ^l *Also at Frontiers Science Center for Rare Isotopes, Lanzhou University, Lanzhou 730000, People's Republic of China*
- ^m *Also at Lanzhou Center for Theoretical Physics, Lanzhou University, Lanzhou 730000, People's Republic of China*